

Chapter III: Vacuolar morphogenesis

Abstract

In this chapter, I found the co-localization of the actin microfilaments (MFs) and vacuolar membrane (VM), as visualized by vital VM staining with FM4-64 in living tobacco BY-GF11 cells. The MFs were intensively localized on the VM surface and at the periphery of the transvacuolar strands (TVSs) rather than at their center. The co-localization of MFs and VMs was confirmed by the observation made using transient expression of RFP-ABD2 in tobacco BY-2 cells stably expressing GFP-AtVAM3 (BY-GV7) and BY-2 cells stably expressing NtTIP1;1-GFP fusion protein (BY-TIPG). Live cell imaging revealed dynamic movement of MF structures that was parallel to that of TVSs. Treatment with an actinpolymerization inhibitor, bistheonellide A (BA), disorganized TVS structures and produced small spherical vacuoles in the VM-accumulating region. Three-dimensional (3-D) reconstructions of the vacuolar structures revealed a disconnection of these small spherical vacuoles from the large vacuoles. Live cell imaging and quantitative image analyses demonstrated rapid movements of MFs and VMs near the cell cortex, which were inhibited by the general myosin ATPase inhibitor, 2,3-butanedion monoxime (BDM). Moreover, both BA and BDM treatment inhibited the reorganization of the TVSs and the migration of daughter cell nuclei at early G1 phase, suggesting a requirement for the acto-myosin system for vacuolar morphogenesis during cell cycle progression. These results suggest that MFs support the vacuolar structures and that the acto-myosin system plays an essential role in vacuolar morphogenesis.

Introduction

Vacuoles are the largest organelles in mature plant cells and play important roles in a variety of plant growth and developmental processes (Wink 1993, Marty 1999). In mature tissues, the large central vacuoles occupy a considerable proportion of the intracellular volume of the plant cells. Whereas the traditional image of the plant vacuole was a large simple sac with a smooth surface, most recent morphological studies on the vacuolar membrane (VM) using vital staining dyes (Emans et al. 2002, Kutsuna and Hasezawa 2002, Ruthardt 2005) and the GFP technique (Saito et al. 2002, Uemura et al. 2002, Kutsuna et al. 2003, Hicks et al. 2004) have demonstrated their complicated structures and dynamic behavior. For instance, within the *Arabidopsis* vacuolar lumen, spherical structures termed 'bulbs' (Saito et al. 2002), and invaginations of intravacuolar sheets (Uemura et al. 2002), as well as tubular structures (Hicks et al. 2004) have been described. Tubular structures of the vacuolar membrane (TVMs) appear surrounding the mitotic apparatus in mitotic BY-2 cells (Kutsuna and Hasezawa 2002, Kutsuna et al. 2003). TVMs, which connect the large vacuoles, were found to be bisected by the cytoplasmic plate in metaphase, suggesting that they were necessary for maintaining the specific conditions of the vacuoles, including osmotic pressure, pH and membrane potential (Kutsuna et al. 2003). Conversely, transvacuolar strands (TVSs), which connect the cytosol on the opposite side of vacuoles, have been identified as a possible route for cytoplasmic streaming, considered responsible for the intracellular transport of molecules and organelles in vacuolated cells (Shimmen and Yokota 1994, Nebenführ et al. 1999, Grolig and Pierson 2000, Tominaga et al. 2000b, Van Gestel et al. 2002, Saito et al. 2005). Therefore, the regulation of vacuolar morphology is crucial for maintaining vacuolar conditions as well as for cytoplasmic homeostasis in mature plant cells.

Pharmacological experiments have suggested the involvement of actin microfilaments (MFs) in determining vacuolar structure and dynamics. Indeed, the actin polymerization inhibitor cytochalasin D (CD) was found to block VM dynamics

in *Arabidopsis* leaf epidermal cells (Uemura et al. 2002). Treatment with the dimeric macrolide, bistheonellide A (BA), which inhibits actin polymerization (Saito et al. 1998), also prevented the structural rearrangements of vacuoles during mitosis and disrupted TVMs in tobacco BY-2 cells (Kutsuna et al. 2003). However, no direct observation of MFs and VMs in living plant cells has been performed, and the relationship between the spatial and temporal localization of MFs and VMs has remained largely unknown.

In the present study, using BY-GF11 cells together with FM4-64 staining, I simultaneously observed the MF and VM structures in living cells without the need for fixation or permeabilization. These observations revealed an intense localization of MFs on the VM and at the periphery of the TVSSs rather than at the center of the TVSSs. Live cell imaging showed parallel behavior of the MFs and the VM structures. Furthermore, both actin and myosin inhibitors were found to block reorganization of the TVSSs at early G1 phase. In the light of these results, I discuss the significance of MFs in vacuolar morphogenesis in plant cells.

Methods

Plant material and synchronization

Cell culture and synchronization of tobacco BY-2 was performed as described in chapter I. In order to obtain higher synchrony during the transition from M phase to G1 phase, 3 μ M propyzamide was added to the cell suspension to induce mitotic arrest at 6 h after release from aphidicolin. When propyzamide was removed after 4 h of treatment by washing with 10 vols of the medium, the cell population showed higher synchrony than with simple treatment with aphidicolin (Nagata et al., 1992).

Transgenic BY-2 cell lines stably expressing a GFP-AtVAM3 (Kutsuna and Hasezawa, 2002) and GFP-ABD2 were previously established (chapter I, Sano and Higaki et al. 2005, Higaki et al. 2006, Higaki et al. 2007a,b, Higaki et al. 2008). The transgenic cell lines could be maintained and synchronized by almost the same

procedure as used for the original BY-2 cell line.

Plasmid construction

Tobacco BY-2 TIP1;1 cDNA was identified based on the nucleotide sequence of *Nicotiana glauca* TIP1;1 (GenBank accession No. AF290619). A PCR fragment of the tobacco BY-2 NtTIP1;1 was amplified with primers of *NtTIP1;1* fw (5'-CACCATGCCGATCA ACCAAATTGCT-3') and *NtTIP1;1* rev (5'-AAAATCTCCACTT GGGAGTGG-3'). To obtain the full-length cDNA, the 5' and 3' cDNA ends were amplified by the RACE technique (SMART™ RACE cDNA Amplification kit, Takara Shuzo Co. Ltd, Otsu, Japan). To create a NtTIP1;1-GFP construct, the PCR-amplified open reading frame region of tobacco NtTIP1;1 was cloned into the pENTR/D/TOPO vector (Invitrogen, Carlsbad, CA, USA) and subsequently into a binary vector of pGWB5 using the Gateway™ system (Invitrogen). The pGWB5 vector that provides a C-terminal GFP fusion protein was kindly provided by Dr. T. Nakagawa of Shimane University.

The RFP-ABD2 construct was created by replacement of the GFP by tdTomato (Shaner et al. 2004) in the cauliflower mosaic virus 35S-sGFP(S65T)-ABD2 vector (see chapter I), resulting in an in-frame fusion of the N-terminus of RFP and the C-terminus of AtFim1 ABD2. The tdTomato vector was kindly provided by Dr. R. Y. Tsien of University of California.

Transformation and establishment of the BY-2 cells stably expressing NtTIP1;1-GFP

The NtTIP1;1-GFP construct was transformed into *Agrobacterium tumefaciens* strain LBA4404. A 4 ml aliquot of 3-day-old BY-2 cells was incubated with 100 µl of the overnight culture of the transformed *A. tumefaciens* as described by An (1985). After 2 d incubation at 27°C, cells were washed four times in 5 ml of LSD medium, then plated onto solid LSD medium containing 500 mg l⁻¹ carbenicillin, 30 mg l⁻¹ kanamycin and 15 mg l⁻¹ hygromycin. Calluses, which appeared after 20 days, were transferred onto new plates and cultured independently until they reached approximately 1 cm in diameter, when they were transferred to 20 ml of

liquid LSD medium and agitated on a rotary shaker at 130 rpm at 27°C in the dark. After 1 month, a cell line suitable for observing VMs was selected by examination of GFP fluorescence by fluorescent microscopy, and the cell line obtained was designated BY-TIPG (Okubo-Kurihara et al. 2009).

Cell staining

To observe MFs in the BY-GV7 cells, rhodamine-phalloidin was used as described in chapter I. To observe the VM in the BY-GF11 cells, N-[3-triethylammoniumpropyl]-4-(6-(4-(diethylamino)phenyl)hexatrienyl)-pyridinium dibromide (FM4-64; Molecular Probes) was added to the cell suspension at a final concentration of 32 μ M. The cells were incubated for 2 min, washed with fresh culture medium, and observed 10-20 hours after FM4-64 pulse labelling as described in Kutsuna and Hasezawa (2002).

Transient expression

A cell suspension of 3-day-old BY-GV7 cells or BY-TIPG cells was filtrated onto filter paper, and the cells bombarded with gold particles (1.0 μ M) coated with the appropriate vector constructs using a particle delivery system (PDS-1000/He, Bio-Rad, Hercules, CA, USA) according to the manufacture's recommendations. Filtrated cells were placed at a distance of 6 cm under the stopping screen and bombarded in a vacuum of 28 in Hg at a helium pressure of 1100 psi. Following bombardment, cells were diluted in LS medium and kept in the dark at 27°C for 6-12 h before observation.

Microscopy

The cells were transferred into 35-mm-diameter Petri dishes with 14-mm-diameter coverslip windows at the bottom (Matsunami Glass Ind. Ltd, Osaka, Japan). The dishes were placed onto the inverted platform of a fluorescence microscope (IX-70; Olympus) equipped with a confocal laser scanning head and control systems (CLSM GB-200; Olympus) or a cooled CCD camera head system

(CoolSNAP HQ, PhotoMetricsInc., Huntington Beach, Canada). Indirect quantification of fluorescence levels was performed using MetaMorph software (Universal Imaging Co., Downingtown, Panama).

Drug treatment

Cells were treated with 3 μ M propyzamide (Wako Pure Chemical Ind., Osaka, Japan) to disrupt the MTs, or with 1 μ M BA (Wako Pure Chemical Ind) or 100 μ M CD (Sigma) to disrupt the MFs. Myosin activity was inhibited by treatment with 30 mM BDM (Sigma).

Three-dimensional (3-D) reconstruction of vacuolar structures

Reconstruction and visualization of the 3-D structures of the vacuoles were performed using REANT, as previously in Kutsuna and Hasezawa (2005). Serial optical sections were taken at 0.5- μ m intervals.

Image analysis for estimation of MF and VM movement

In order to estimate the movement of MFs and VMs, I performed correlation analysis in which alterations in the images were determined using the normalized correlation coefficient ($Corr_{norm}$) between the first time-sequential image and subsequent images. $Corr_{norm}$ is defined by:

$$Corr_{norm} = \frac{\sum_{x,y} (f(x,y) - \bar{f})(g(x,y) - \bar{g})}{\sqrt{\sum_{x,y} (f(x,y) - \bar{f})^2 \sum_{x,y} (g(x,y) - \bar{g})^2}}$$

where f is the first image in the time-sequential images, \bar{f} is the mean of $f(x, y)$, g is the subsequent image, and \bar{g} is the mean of $g(x, y)$. When images remained unchanged during observation, i.e. the MFs or VMs did not move, $Corr_{norm}$ attained a value of 1. When the images were completely different, the $Corr_{norm}$ attained a value of 0. A decline in $Corr_{norm}$ from a value of 1 to 0 represented a measure of MF or VM movement. To improve the signal to noise ratio, a Gaussian filter was applied to all the time-sequential images obtained by confocal laser scanning

microscopy (CLSM) before calculation of $Corr_{norm}$. The calculation of $Corr_{norm}$ was performed using the Java plug-in; stkCorr on ImageJ (Abramoff et al. 2004). This plug-in is available from Kashiwa BioImaging website (<http://hasezawa.ib.k.u-tokyo.ac.jp/zp/Kbi>).

Results

Dual visualization of MFs and VMs in living plant cells

It has been possible to simultaneously observe MFs and VM using tobacco BY-GV7 cells, in which the VM was labeled by GFP-AtVAM3, and the saponin-permeabilizing rhodamine-phalloidin staining method (Fig. III-1A, B, C) as reported previously (Kutsuna et al. 2003). However, because of the sensitivity of the MFs and VMs to saponin, not all cells were suitable for observation by this staining method.

Therefore, I used the BY-GF11 cells and fluorescent dye FM4-64 for simultaneous imaging of MFs and VM structures without cell membrane permeabilizing treatment. As mentioned in chapter II, FM4-64 is a vital endocytic tracer, and finally reaches the VM (Kutsuna and Hasezawa 2002, Bolte et al. 2004, Samaj et al. 2005). From 10 to 20 hours after pulse-labeling with 32 μ M FM4-64, I observed that the fluorescence specifically localized in VM in BY-GF11 cells (Fig. III-1F) as previously reported in untransformed BY-2 cells (Kutsuna and Hasezawa 2002). For VM observations, all results presented in this chapter were from those conducted 10-20 hours after pulse-labeling. Using this vital VM staining technique in the BY-GF11 cells, I succeeded in carrying out dual observations of the MFs and VMs in living cells without any adverse side effects (Fig. III-1D, E, F).

Localization of MFs and VMs in living tobacco BY-2 cells

To examine in detail the spatial configuration of MFs and VMs, I observed the dual visualized cells using CLSM. In living BY-GF11 cells stained with FM4-64, I found that the MFs localized close to the cell cortex (Fig. III-2A, B, C, D, small

arrows; Fig. III-2E), vacuolar surface (Fig. III-2A, B, C, D, large arrows; Fig. III-2E) and along the TVSs (Fig. III-2A, B, C, D, arrowheads; Fig. III-2F). The latter two localizations were confirmed by FM4-64 staining (compare the large and small arrows in Fig. III-2C). An intensity profile across the vacuolar surface and cell cortex showed that the MFs localized on the vacuolar surface more intensively (Fig. III-2G, large arrow) than close to the cell cortex (Fig. III-2G, small arrow). In the TVSs, MFs seemed to localize at the periphery of the strands rather than at the center of strands (Fig. III-2D, R-S). An intensity profile across the TVSs revealed the close localization of the MFs and VMs (Fig. III-2H).

To confirm the above co-localization of MFs and VMs, I transiently expressed red fluorescent protein (RFP)-ABD2 in tobacco BY-GV7 cells. The fluorescence of RFP-ABD2 and GFP-AtVAM3 was localized close together on the TVSs (Fig. III-2I, J, K), which was in agreement with that found using GFP-ABD2 and FM4-64. In addition, I generated a transgenic tobacco BY-2 cell line that stably expresses GFP fusions to tonoplast intrinsic protein (NtTIP1;1-GFP; Okubo-Kurihara et al. 2009). In *Arabidopsis*, NtTIP1;1-GFP localized on the VMs and endoplasmic reticulum and is used as another marker of the VM (Mitsuhashi et al. 2000, Saito et al. 2002). Confocal images of my transgenic cell line named BY-TIPG (BY-2 cells stably expressing NtTIP1;1-GFP) confirmed the co-localization of the VMs and the MFs which were visualized by the transient expression of RFP-ABD2 (Fig. III-2L, M, N).

Dynamic movement of TVSs and MF structures

Since the above dual localization suggested a role for MFs in TVS organization, I performed a live cell imaging of the TVS movement. Bright field observation showed a rapid movement of the TVSs that was also reported in other systems (Emans et al. 2002, Uemura et al. 2002, Hoffmann and Nebenführ 2004, Ruthardt 2005). According to the TVS movements, fluorescent images of the GFP-ABD2 revealed parallel movements of the MFs (Fig. III-3A, B, C, arrows). In addition, fluorescent spots of GFP-ABD2 were moving on the surface of the large vacuole, which was confirmed by bright field imaging (Fig. III-3C, arrowheads).

Together with the co-localization of MFs and VMs, these observations implied the importance of the motility of the MFs for the vacuolar movement.

Deformation of MFs and VMs after application of actin polymerization inhibitor

To confirm the relationship between MF and VM structures in the TVSs, I examined the effect of BA, an inhibitor of actin polymerization. The TVSs, which ran through the large vacuole, were evident before BA addition (Fig. III-4A, 0 min, arrows). After BA application, the MFs and TVSs gradually began to shrink synchronously (Fig. III-4A, 15-45 min) and completely disappeared 45 min after BA addition. After the disruption of the TVSs, the small spherical vacuoles appeared from the region in which VM accumulated (Fig. III-4A, 45-60 min, arrowheads). The disruption of the TVSs and the appearance of the small spherical vacuoles were also observed in both BY-TIPG cells (Fig. III-4B) and BY-GV7 cells (Fig. III-6B). 3-D reconstructions of the vacuolar structures from serial images obtained by CLSM, using REANT software (Kutsuna and Hasezawa 2005), demonstrated that these small spherical vacuoles were disconnected from the large vacuoles (Fig. III-4C, arrowheads).

To confirm these phenomena observed by the above live cell imaging statistically, I counted cells with TVSs or small spherical vacuoles. Upon BA treatment, most of the TVSs disappeared, while an inhibitor of microtubule (MT) organization, propyzamide, had almost no effect (Fig. III-4D). BA treatment also produced small spherical vacuoles in >80% of the cells, but these structures were never observed in the control and propyzamide-treated cells (Fig. III-4E).

Active movement of the MFs and VMs near the cell cortex

Since MFs seemed to be involved in the active movement of the TVSs, I next focused on the movement of the MF arrays near the large vacuolar surface. Projection of time-sequential images taken every 30 sec showed dynamic movements of MFs near the large vacuolar surface (Fig. III-5A, C). In particular, some MFs were constantly swinging (Fig. III-5E). To examine the role of myosin on the

movement of MFs, I treated cells with the general myosin ATPase inhibitor, 2,3-butanedion monoxime (BDM) (Tominaga et al. 2000a). Treatment of BY-GF11 cells with 30 mM BDM for 30 min maintained the structure of MFs but completely blocked their movements (Fig. III-5B, D). When I quantified the MF movement using a correlation coefficient as an indicator of the alteration of images (see Methods), BDM treatment clearly inhibited the MF movement. Like the MF movements, when I monitored VM movement in tobacco BY-GV7 cells, the surface of the large vacuole was found to be constantly moving (Fig. III-6A, D). This movement was inhibited by both BA and BDM treatment (Fig. III-6E, F, G), but BA treatment additionally produced small spherical vacuoles, whereas BDM treatment did not change the VM structure essentially (Fig. III-6B, C).

Acto-myosin is involved in vacuolar morphogenesis at early G1 phase

Vacuolar structures dynamically change during cell cycle progression (Kutsuna and Hasezawa 2002, Kutsuna et al. 2003). In mitosis, most of the TVSSs disappeared but became reorganized at early G1 phase (Hasezawa and Kumagai 2002, Kutsuna and Hasezawa 2002). To examine the role of MFs in vacuolar dynamics during cell cycle progression, I observed synchronized BY-GF11 cells stained with FM4-64 in particular from telophase to early G1 phase. At late telophase, very few MFs were observed in intravacuolar sheets (Fig. III-7A, 0 min), but the MFs started to elongate along the intravacuolar sheets during the migration of the daughter nuclei in early G1 phase, (Fig. III-7A, 15 and 25 min, arrowheads). Finally, TVSSs with intensive MF localization could be recognized (Fig. III-7A, 30 min, arrow). To investigate the involvement of acto-myosin in the formation of the TVSSs, BA or BDM was applied at late telophase. Reorganization of TVSSs was not observed, and migration of daughter nuclei was completely inhibited (Fig. III-7B, C, D, E). In this stage of the cell cycle, bundle-like MF structures were accumulated near the cell surface and, immediately below the MF bundle, a VM structure was observed (Fig. III-8A, arrows). 3-D reconstructions of the vacuoles clearly showed the groove-like structure of the VM at early G1 phase (Fig. III-8B, arrows). If these

VM structures are an origin of the TVSs, the MF structures may be involved in the origination of the TVSs in addition to their elongation and maintenance.

Discussion

MFs localized on the VM; possible roles in maintenance of vacuolar structure

In this study, I clearly demonstrated the intensive localization of MFs on the surface of the VM in tobacco BY-GF11 cells stained with the vital staining dye, FM4-64 (Fig. III-2). In particular, I found that the MFs localized at the periphery of the TVSs rather than at the center, which was confirmed by transient expression of RFP-ABD2 in tobacco BY-GV7 and BY-TIPG cells (Fig. III-2F, H, J, K, M, N). My observations suggested a role for the MFs in mechanically supporting the strand structures of the VM. Indirectly, this role has been suggested by several pieces of evidence: in *Tradescantia* stamen hair cells, microinjection of profilin induced an irreversible change in the TVSs in addition to the degradation of MFs (Staiger et al. 1994, Valster et al. 1997). The disappearance of the TVSs and the disorganization of the MF bundles was also observed in *Hydrocharis dubia* root hair cells microinjected with antiserum against a 135 kDa actin-bundling protein, a villin homolog (Tominaga et al. 2000b).

Disruption of the MFs deformed the TVSs (Fig. III-4), which suggested their role in the maintenance of the TVSs. After the deformation of the TVSs, small spherical vacuoles appeared (Figs. III-3, III-4). These structures were reported to exist around the nuclei in the MF-disrupted BY-2 cells at late G2 and metaphase, and in Lat B-treated or arp2 *Arabidopsis* mutant trichomes (Kutsuna et al. 2003, Mathur et al. 2003). Since the localization of FM4-64 or GFP-AtVAM3 fluorescence was limited to the VM of large vacuoles before BA addition (Figs. III-4A, B), these small spherical vacuoles seemed to be derived from the 'excessive' VM of large vacuoles by the disruption of the strand structures.

By using saponin-permeabilizing methods, it was reported that TVMs partially co-localize with the MF network (Kutsuna et al. 2003), suggesting that MFs

play important roles in supporting not only strand structures but also tubular structures of the VM. Using an *in vitro* system, actin-containing vesicles demonstrated that MFs could maintain protrusive membrane structures (Miyata et al. 2000). I speculate that bundles or networks of MFs play a role in stabilizing the strand or tubular structures of the VM against various forces, such as VM tension or the osmotic stress. The establishment of *in vitro* observation systems with isolated vacuoles and MFs in future studies might be used to evaluate this notion.

Dynamic arrangement of MFs and vacuolar movement

I found that MFs along the TVSs and on the large vacuoles underwent dynamic movement in living BY-GF11 cells (Figs. III-3, III-5). Although MF movement in *Tradescantia* stamen hair cells microinjected with fluorescent labeled AtFim1 has been reported (Kovar et al. 2001), their movement in plant cells has remained largely unknown. My live cell imaging, together with correlation analyses, revealed that the general myosin ATPase inhibitor, BDM, inhibited cortical MF movement in living plant cells. These results imply that myosin movement along MFs is involved in MF movement in plant cells. The observation that an application of both heavy meromyosin and Mg^{2+} -ATP made the thermal bending motion of MFs faster and larger (Yanagida et al. 1984) supports my findings.

Application of BDM essentially did not affect the configuration of the TVSs (Fig. III-6C), suggesting that myosin activity is not required for the maintenance of the strand structures. In contrast, BDM treatment inhibited both the VM movements (Fig. III-6F, G) and the conversion of intravacuolar sheets to TVSs (Fig. III-7C, E). My results suggested the involvement of the acto-myosin system in the rearrangement of the TVSs. Similar observations were reported in *Arabidopsis* epidermal cells upon CD treatment and for BDM in BY-2 cells (Uemura et al. 2002, Hoffmann and Nebenführ 2004). Recent proteome analysis detected cytoskeleton-related proteins including myosins in isolated vacuoles from *Arabidopsis* (Carter et al. 2004). My results taken together with these observations

strongly suggest the involvement of acto-myosin in vacuolar morphogenesis. In budding yeast, directional movement of vacuoles to the budding site is driven by the acto-myosin system. The vacuole movement depends on Vac17p, which was identified as a component of the vacuole-specific receptor for Myo2p (Tang et al. 2003, Ishikawa et al. 2003). Recently, KAM1/MUR3 protein was identified as a component connecting with MFs and plant Golgi stacks (Tamura et al. 2005). The molecules that connect the MFs and vacuoles have not yet been identified in plants, but clarifying this issue will be crucial in furthering my understanding of the relationship between the MFs and vacuoles.

Possible model of reorganization of TVSs at early G1 phase

In my observation system, it was demonstrated that TVSs were formed from intravacuolar sheets (Fig. III-7A). This conversion of intravacuolar sheets to the TVSs was also suggested by a recent report in BY-2 cells stained with FM dyes (Ruthardt et al. 2005). In addition, my observation suggested the role of the MFs in the TVS reorganization; I found groove-like structures of VMs which existed immediately below the MF bundle-like structures at early G1 phase (Fig. III-8). This finding leads me to propose a possible model for the reorganization of the TVSs. At early G1 phase, the MFs accumulate and organize the bundle-like structure on the large vacuolar surface (Fig. III-9, step 1). The bundle-like structure may invaginate into the vacuolar lumen and form the VM groove (Fig. III-9, step 2). Subsequently, the groove-like VM may continue to invaginate with the MFs and, finally, folding of the invagination produces the TVSs in the vacuolar lumen (Fig. III-9, step 3). Although I have no direct evidence at this moment to clarify the transition of the steps, two types of model have been proposed for the formation of the vacuolar luminal structures (Saito et al. 2002, Uemura et al. 2002). One model supposed small membrane compartments that were engulfed by a large vacuole and formed vacuolar luminal structures. The other model supposed an invagination and folding of the large vacuole. Since I did not find typical small membrane compartments near the vacuolar surface, the TVSs may originate from the large VM

by invagination and folding. However, to clarify the mode of the VM movement to the TVSs and the role of the MFs in this process, further studies are necessary.

Acto-myosin-based vacuolar morphogenesis is crucial for intracellular architecture

It is generally considered that the intracellular architecture cannot undergo drastic changes without vacuolar morphogenesis since the large vacuoles constitute a considerable proportion of the plant cell volume. In this study, I showed that migration of the daughter cell nuclei at early G1 phase was blocked by BA or BDM treatment (Fig. III-7B, C, D) but unaffected by propyzamide treatment. Migration of daughter cell nuclei, at this stage, is crucial for the intracellular event for preparation for the following cell division or cell elongation. The nuclear movement during the G1 to S phase transition required MFs but not MTs (Miyake et al. 1997). In *Arabidopsis* root hairs, to maintain the nuclear position with respect to the growing apex, the MFs, but not the MTs, were required again (Ketelaar et al. 2002). In contrast, the pre-mitotic migration of the nucleus at G2 phase required both MFs and MTs (Katsuta et al. 1990). These reports suggest that the dependence of the cytoskeletons on the nuclear migration is different depending on the stage of the cell cycle. Focused on the roles of vacuolar structures in nuclear migration, TVMs that are located between the cell plate and the daughter cell nuclei and for which there is a possibility to develop into the large vacuoles (Kutsuna et al. 2003, Fig. III-7A) may contribute mechanically as a possible route for the daughter cell nuclear migration.

References

- Abramoff MD, Magelhaes PJ, Ram SJ. (2004) Image processing with Image. *J. Biophotonics Int.* 11:36-42.
- An G. (1985) High efficiency transformation of cultured tobacco cells. *Plant Physiol.* 79:568-570.
- Bolte S, Talbot C, Boutte Y, Catrice O, Read ND, Satiat-Jeunemaitre B. (2004) FM-dyes as experimental probes for dissecting vesicle trafficking in living plant cells. *J. Microscopy* 214:159-173.
- Carter C, Pan S, Zouhar J, Avila EL, Girke T, Raikhel NV. (2004) The vegetative vacuole proteome of *Arabidopsis thaliana* reveals predicted and unexpected proteins. *Plant Cell* 16:3285-3303.
- Emans N, Zimmermann S, Fischer R. (2002) Uptake of a fluorescent marker in plant cells is sensitive to brefeldin A and wortmannin. *Plant Cell* 14:71-86.
- Grolig F, Pierson ES. (2000) Cytoplasmic streaming: from flow to track. In Staiger C, Baluska F, Volkmann P, Barlow P (Eds.). *Actin: A Dynamic Framework for Multiple Plant Cell Functions* (Kluwer Academic, Dordrecht) pp.165-190.
- Hasezawa S, Kumagai F. (2002) Dynamic changes and the role of the cytoskeleton during the cell cycle in higher plant cells. *Int. Rev. Cytol.* 214:161-191.
- Hicks GR, Rojo E, Hong S, Carter DG, Raikhel NV. (2004) Geminating pollen has tubular vacuoles, displays highly dynamic vacuole biogenesis, and requires VACUOLESS1 for proper function. *Plant Physiol.* 134:1227-1239.
- Higaki T, Goh T, Hayashi T, Kutsuna N, Kadota Y, Hasezawa S, Sano T, Kuchitsu K. (2007) Elicitor-induced cytoskeletal rearrangement relates to vacuolar dynamics and execution of cell death: *in vivo* imaging of hypersensitive cell death in tobacco BY-2 cells. *Plant Cell Physiol.* 48: 1414-1425.
- Higaki T, Kutsuna N, Okubo E, Sano T, Hasezawa S. (2006) Actin microfilaments regulate vacuolar structures and dynamics: dual observation of actin microfilaments and vacuolar membrane in living tobacco BY-2 cells. *Plant Cell Physiol.* 47: 839-852.

- Higaki T, Kutsuna N, Sano T, Hasezawa S. (2008) Quantitative analysis of changes in actin microfilament contribution to cell plate development in plant cytokinesis. *BMC Plant Biol.* 8:80.
- Higaki T, Sano T, Hasezawa S. (2007) Actin microfilament dynamics and actin side-binding proteins in plants. *Curr. Opin. Plant Biol.* 10:549-556.
- Hoffmann H, Nebenführ A. (2004) Dynamic rearrangements of transvacuolar strands in BY-2 cells imply a role of myosin in remodeling the plant actin cytoskeleton. *Protoplasma* 224:201-210.
- Ishikawa K, Catlett NL, Novak JL, Tang F, Nau JJ, Weisman LS. (2003) Identification of an organelle-specific myosin V receptor. *J. Cell Biol.* 160:887-897.
- Katsuta J, Hashiguchi Y, Shibaoka H. (1990) The role of the cytoskeleton in positioning of the nucleus in premitotic tobacco BY-2 cells. *J. Cell Sci.* 95:413-422.
- Ketelaar T, Faivre Moskalenko C, Esseling JJ, de Ruijter NC, Grierson CS, Dogterom M, Emons AM. (2002) Positioning of nuclei in *Arabidopsis* root hairs: an actin-regulated process of tip growth. *Plant Cell* 14:2941-2955.
- Kovar DR, Gibbon BC, McCurdy DW, Staiger CJ. (2001) Fluorescently-labeled fimbrin decorates a dynamic actin filament network in live plant cells. *Planta* 213:390-395.
- Kutsuna N, Hasezawa S. (2002) Dynamic organization of vacuolar and microtubule structures during cell cycle progression in synchronized tobacco BY-2 cells. *Plant Cell Physiol.* 43:965-973.
- Kutsuna N, Hasezawa S. (2005) Morphometrical study of plant vacuolar dynamics in single cells using 3-D reconstruction from optical sections. *Microsc. Res. Tech.* 68:296-306.
- Kutsuna N, Kumagai F, Sato MH, Hasezawa S. (2003) 3-D reconstruction of tubular structure of vacuolar membrane throughout mitosis in living tobacco cells. *Plant Cell Physiol.* 44:1045-1054.
- Marty F. (1999) Plant vacuoles. *Plant Cell* 11:587-599.
- Mathur J, Mathur N, Kernebeck B, Hulskamp M. (2003) Mutations in actin-related proteins 2 and 3 affect cell shape development in *Arabidopsis*. *Plant Cell*

15:1632-1645.

- Mitsuhashi N, Shimada T, Mano S, Nishimura M, Hara-Nishimura I. (2000) Characterization of organelles in the vacuolar-sorting pathway by visualization with GFP in tobacco BY-2 cells. *Plant Cell Physiol.* 41:993-1001.
- Miyake T, Hasezawa H, Nagata T. (1997) Role of cytoskeletal components in the migration of nuclei during the cell cycle transition from G1 phase to S phase of tobacco BY-2 cells. *J. Plant Physiol.* 150:528-536.
- Miyata H, Ohki K, Marriott G, Nishiyama S, Akashi K, Kinoshita K. (2000) Cell deformation mechanism studied with actin-containing giant vesicles, a cell-mimicking system. In Luisi PL and Walde P (Eds.). *Giant Vesicles* (John Wiley and Sons, Chichester, UK) pp.319-333.
- Nagata T, Nemoto Y, Hasezawa S. (1992) Tobacco BY-2 cell line as the 'Hela' cell in the cell biology of higher plants. *Int. Rev. Cytol.* 132:1-30.
- Nebenführ A, Gallagher LA, Dunahay TG, Frohlick JA, Mazurkiewicz AM, Meehl JB, Staehelin LA. (1999) Stop-and-go movements of plant Golgi stacks are mediated by the acto-myosin system. *Plant Physiol.* 121:1127-1142.
- Okubo-Kurihara E, Sano T, Higaki T, Kutsuna N, Hasezawa S. (2009) Acceleration of vacuolar regeneration and cell growth by overexpression of an aquaporin NtTIP1;1 in tobacco BY-2 cells. *Plant Cell Physiol.* in press. doi:10.1093/pcp/pcn181
- Ruthardt N, Gulde N, Spiegel H, Fischer R, Emans N. (2005) Four-dimensional imaging of transvacuolar strand dynamics in tobacco BY-2 cells. *Protoplasma* 225:205-215.
- Saito C, Morita MT, Kato T, Tasaka M. (2005) Amyloplasts and vacuolar membrane dynamics in the living graviperceptive cell of the *Arabidopsis* inflorescence stem. *Plant Cell* 17:548-558.
- Saito C, Ueda T, Abe H, Wada Y, Kuroiwa T, Hisada A, Furuya M, Nakano A. (2002) A complex and mobile structure forms a distinct subregion within the continuous vacuolar membrane in young cotyledons of *Arabidopsis*. *Plant J.* 29:245-255.
- Saito S, Watabe S, Ozaki H, Kobayashi M, Suzuki T, Kobayashi H, Fusetani N,

- Karaki H. (1998) Actin-depolymerizing effect of dimeric macrolides, bistheonellide A and swinhilide A. *J. Biochem.* 123:571-578.
- Samaj J, Read ND, Volkmann D, Menzel D, Baluska F. (2005) The endocytic network in plants. *Trends Cell Biol.* 15:425-433.
- Sano T, Higaki T, Oda Y, Hayashi T, Hasezawa S. (2005) Appearance of actin microfilament 'twin peaks' in mitosis and their function in cell plate formation, as visualized in tobacco BY-2 cells expressing GFP-fimbrin. *Plant J.* 44: 595-605.
- Shaner NC, Campbell RE, Steinbach PA, Giepmans BN, Palmer AE, Tsien RY. (2004) Improved monomeric red, orange and yellow fluorescent proteins derived from *Discosoma* sp. red fluorescent protein. *Nat. Biotechnol.* 22:1567-1572.
- Shimmen T, Yokota E. (1994) Physiological and biochemical aspects of cytoplasmic streaming. *Int. Rev. Cytol.* 155:97-139.
- Staiger CJ, Yuan M, Valenta R, Shaw PJ, Warn RM, Lloyd CW. (1994) Microinjected profilin affects cytoplasmic streaming in plant cells by rapidly depolymerizing actin microfilaments. *Curr. Biol.* 4:215-219.
- Tamura K, Shimada T, Kondo M, Nishimura M, Hara-Nishimura I. (2005) KATAMARI1/MURUS3 is a novel Golgi membrane protein that is required for endomembrane organization in *Arabidopsis*. *Plant Cell* 17:1764-1776.
- Tang F, Kauffman EJ, Novak JL, Nau JJ, Catlett NL, Weisman LS. (2003) Regulated degradation of a class V myosin receptor directs movement of the yeast vacuole. *Nature* 422:87-92.
- Tominaga M, Yokota E, Sonobe S, Shimmen T. (2000a) Mechanism of inhibition of cytoplasmic streaming by a myosin inhibitor 2,3-butanedione monoxime. *Protoplasma* 213:46-54.
- Tominaga M, Yokota E, Vidali L, Sonobe S, Hepler PK, Shimmen T. (2000b) The role of plant villin in the organization of the actin cytoskeleton, cytoplasmic streaming and the architecture of the transvacuolar strand in root hair cells of *Hydrocharis*. *Planta* 210:836-843.
- Uemura T, Yoshimura SH, Takeyasu K, Sato MH. (2002) Vacuolar membrane dynamics revealed by GFP-AtVam3 fusion protein. *Genes Cells* 7:743-753.

- Valster AH, Pierson ES, Valenta R, Hepler PK, Emons A. (1997) Probing the plant actin cytoskeleton during cytokinesis and interphase by profilin microinjection. *Plant Cell* 9:1815-1824.
- Van Gestel K, Kohler RH, Verbelen JP. (2002) Plant mitochondria move on F-actin, but their positioning in the cortical cytoplasm depends on both F-actin and microtubules. *J. Exp. Bot.* 53:659-667.
- Wink M. (1993) The plant vacuole: a multifunctional compartment. *J. Exp. Bot.* Suppl. 44:231-246.
- Yanagida T, Nakase M, Nishiyama K, Oosawa F. (1984) Direct observation of motion of single F-actin filaments in the presence of myosin. *Nature* 307:58-60.

Figures

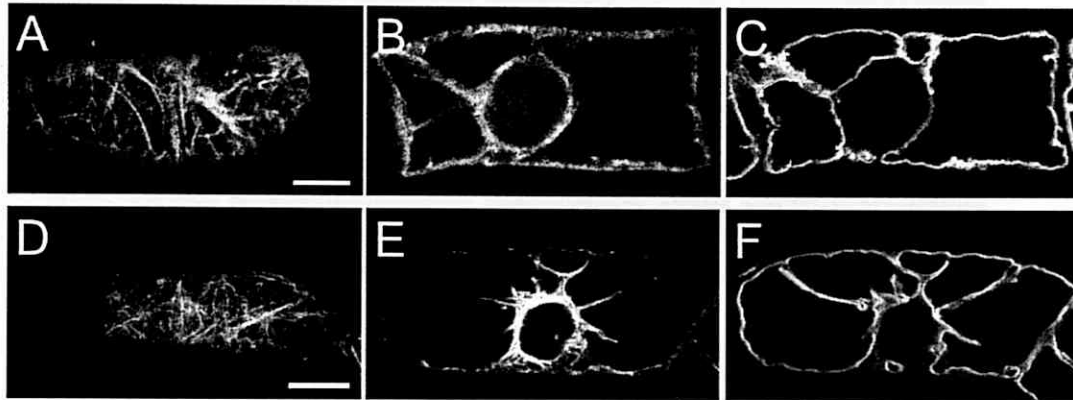


Figure III-1. Dual visualization of MFs and VMs in living BY-2 cells. (A, B) MFs were visualized by rhodamine-phalloidin in the cortex (A) and mid-plane (B) after saponin pre-treatment. (C) VM structures in the same plane as (B) were visualized by GFP-AtVAM3. The slightly deformed VM structures were possibly due to the permeabilization process. (D, E) The MFs were clearly labeled by GFP-ABD2 in the cortex (D) and mid-plane (E) of the BY-GF11 cell line. (F) VM structures could be visualized in the same plane as (E), as in normal cells, by vital staining with FM4-64. Scale bars: 10 μ m.

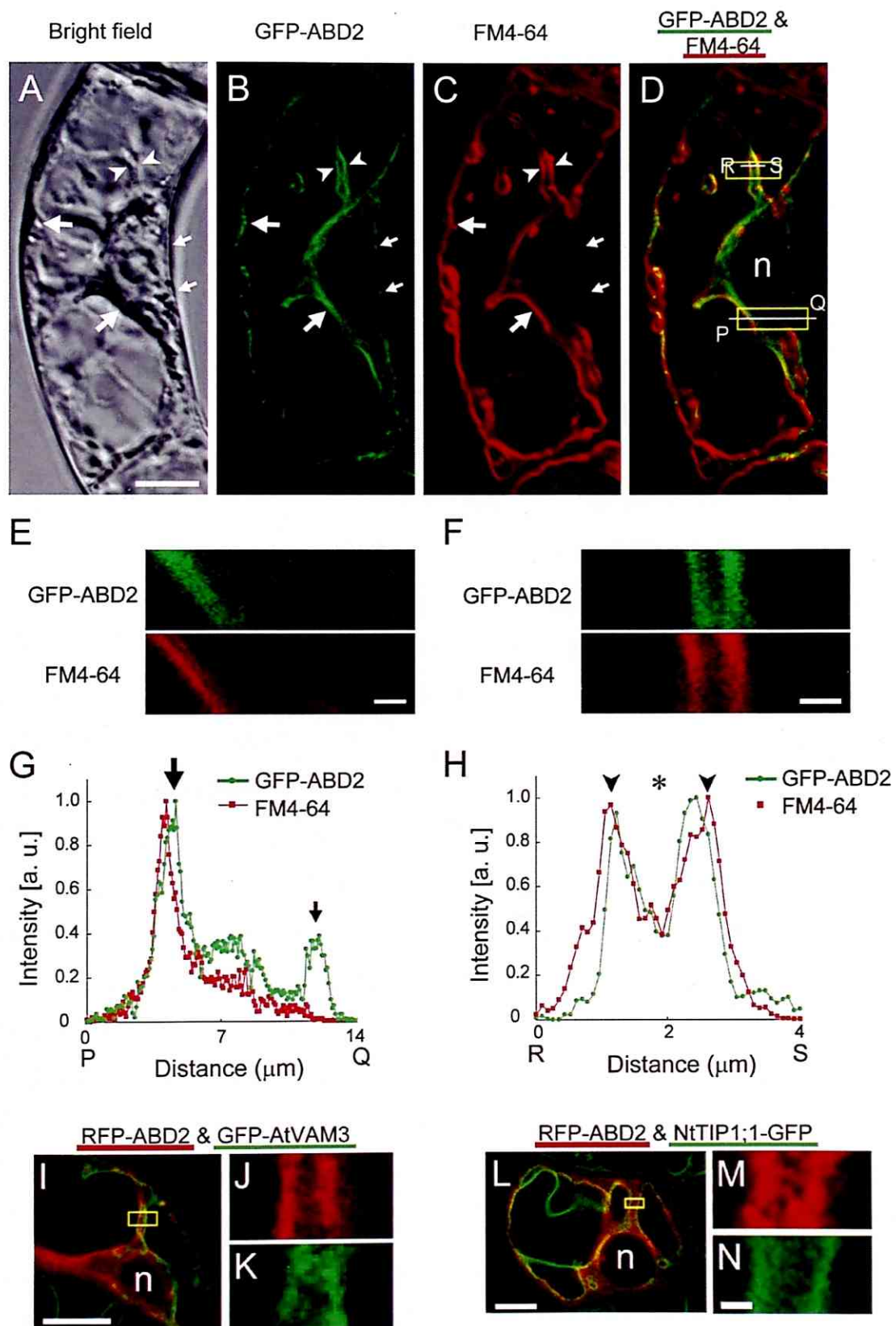


Figure III-2. Localization of MFs and VMs in living BY-2 cells. (A-C) A BY-GF11 cell was observed by CLSM in bright field (A), and by GFP-ABD2 (B) and FM4-64 (C). Cortical MFs (small arrows) and the MFs close to the VM (large arrows) were observed. In the transvacuolar strands (TVSs), the MFs were localized close to the VM and at the periphery of the strands (arrowheads). Scale bar: 10 μ m. (D) An overlay image of (B) and (C). (E, F) Magnified separated images of the large (E) and small (F) boxed region in (D). Scale bars: 2 μ m. (G) An intensity profile of GFP-fluorescence and FM4-64 along the P-Q axis in (D). The small and large arrows indicate the GFP signal of the cortical MFs and on the vacuolar surface, respectively. (H) An intensity profile along the R-S axis, across the cytoplasmic strand, in (D). Arrowheads indicate the periphery of the strand, and the asterisk indicates the center of the strand. (I) A BY-GV7 cell transiently expressing RFP-ABD2. Green and red colors show GFP-AtVAM3 and RFP-ABD2, respectively. Scale bar: 10 μ m. (J, K) Magnified separated images of the boxed region in (I) of the RFP-ABD2 fluorescence (J) and that of GFP-AtVAM3 (K). Scale bar: 2 μ m. (L) A BY-TIPG cell transiently expressing RFP-ABD2. Green and red colors show NtTIP1;1-GFP and RFP-ABD2, respectively. Scale bar: 10 μ m. (M, N) Magnified separated images of the boxed region in (L) of the RFP-ABD2 fluorescence (M) and that of NtTIP1;1-GFP (N). Scale bar: 2 μ m.

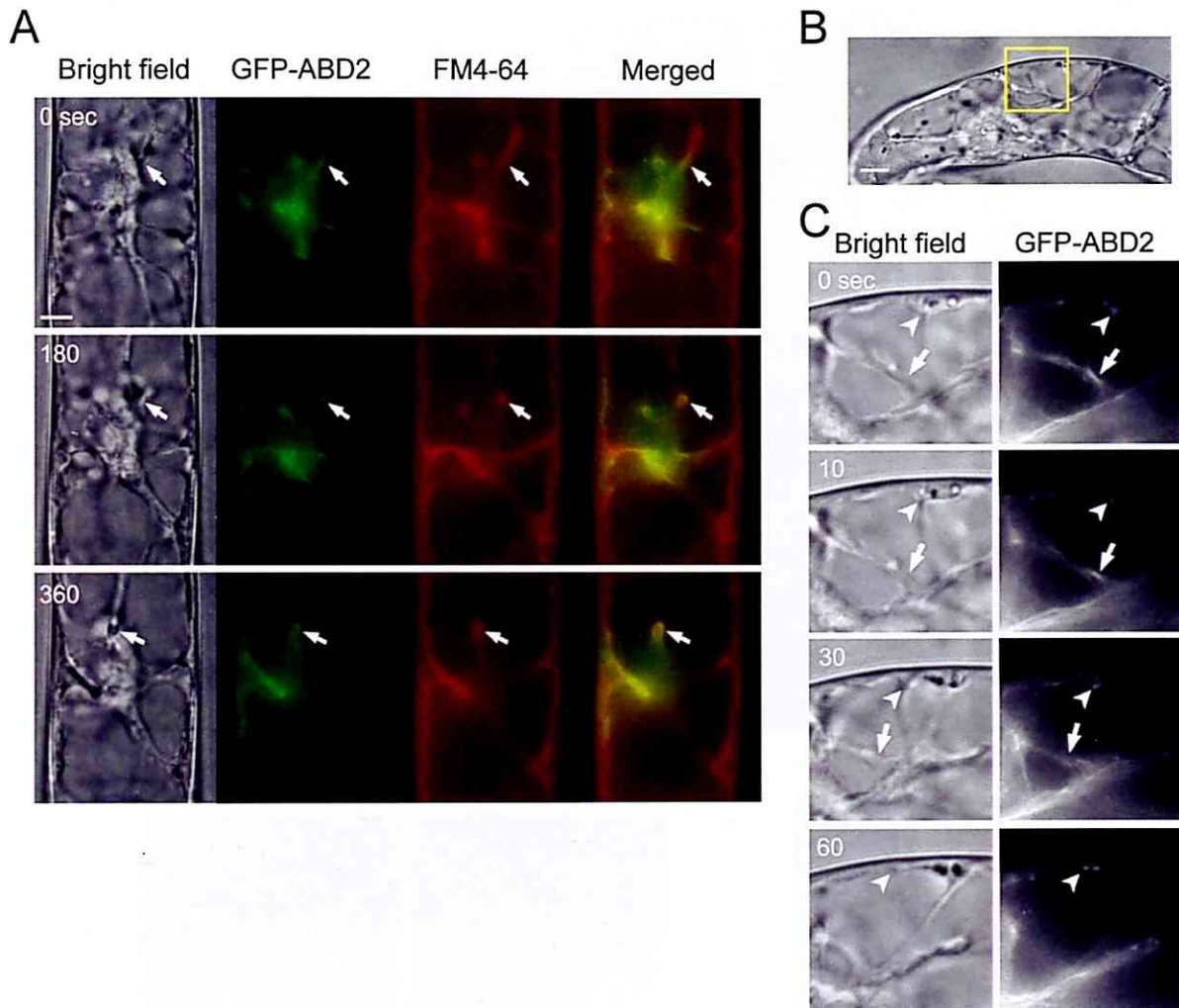


Figure III-3. Time-sequential images of the movement of MFs along cytoplasmic strands. (A) Images of a BY-GF11 cell stained with FM4-64 were obtained every 180 sec, and the bright field, GFP-ABD2 and FM4-64 images are shown. The rightmost images show the merged images of GFP-ABD2 and FM4-64. Motile transvacuolar strands (TVSs) and MFs (arrows) were observed. (B) A bright field image of a BY-GF11 cell. (C) Magnified and time-sequential images of the boxed region in (B). Arrows show a TVS. On the large vacuolar surfaces, a bright spot of GFP-ABD2 was sliding (arrowheads). Scale bar: 10 μ m.

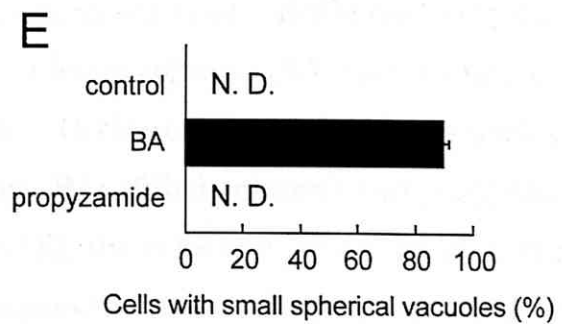
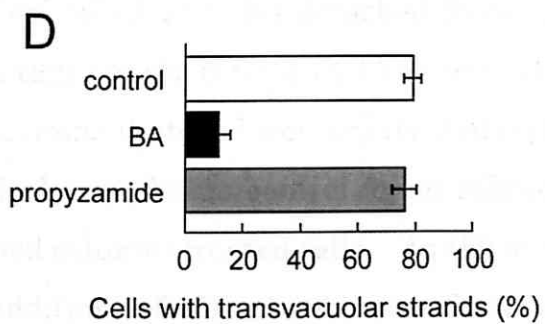
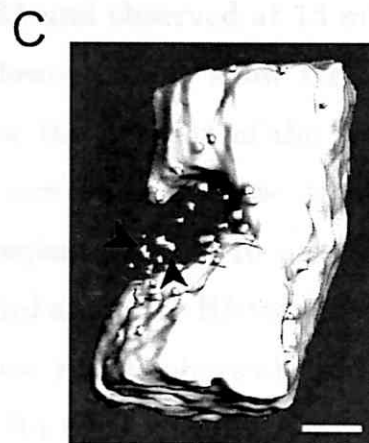
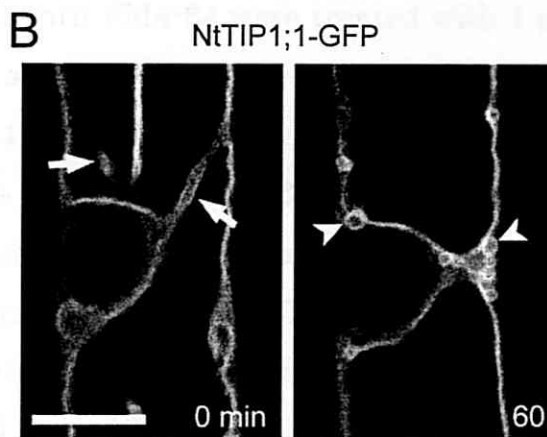
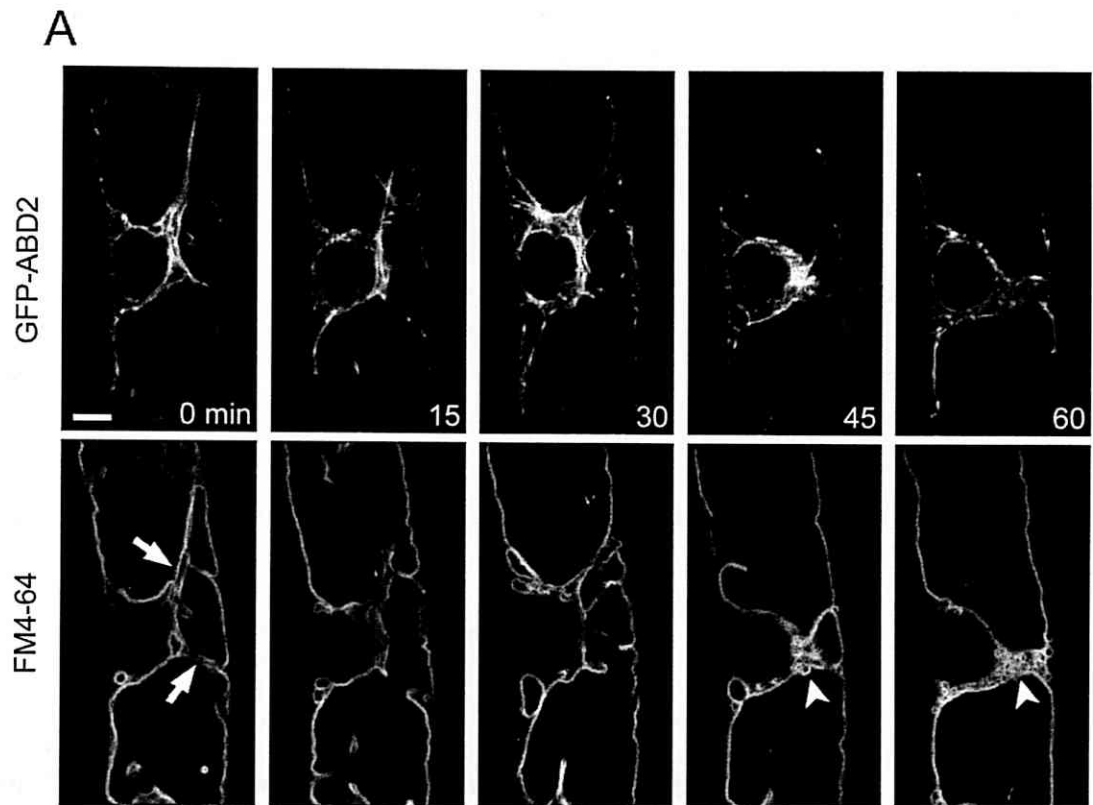


Figure III-4. Vacuolar deformation induced by BA treatment. (A) BY-GF11 cells stained with FM4-64 were treated with 1 μ M BA and observed at 15 min intervals under a fluorescent microscope. Upper and lower panels show GFP-ABD2 and FM4-64 images, respectively. The arrows show the position of the transvacuolar strands (TVSs) before BA treatment. The arrowheads show small spherical vacuoles appearing in the VM-accumulating region. Bar = 10 μ m. (B) Vacuolar structures visualized in BY-GG cells before (0 min) and after BA treatment (60 min). The arrows show the TVS, and arrowheads show small spherical vacuoles. Scale bar: 10 μ m. (C) A 3-D image of vacuoles in a BA-treated cell. Arrowheads show small spherical vacuoles detached from the large vacuole. Scale bar: 10 μ m. (D) Percentages of the cells with TVSs in control (open column), BA- (filled column) and propyzamide-(hatched column) treated cells. (E) Percentages of the cells with small spherical vacuoles in control (open column), BA- (filled column) and propyzamide-(hatched column) treated cells. In (D) and (E), the cells were observed 60 min after the addition of the inhibitors. Bars represent the standard error of three independent experiments.

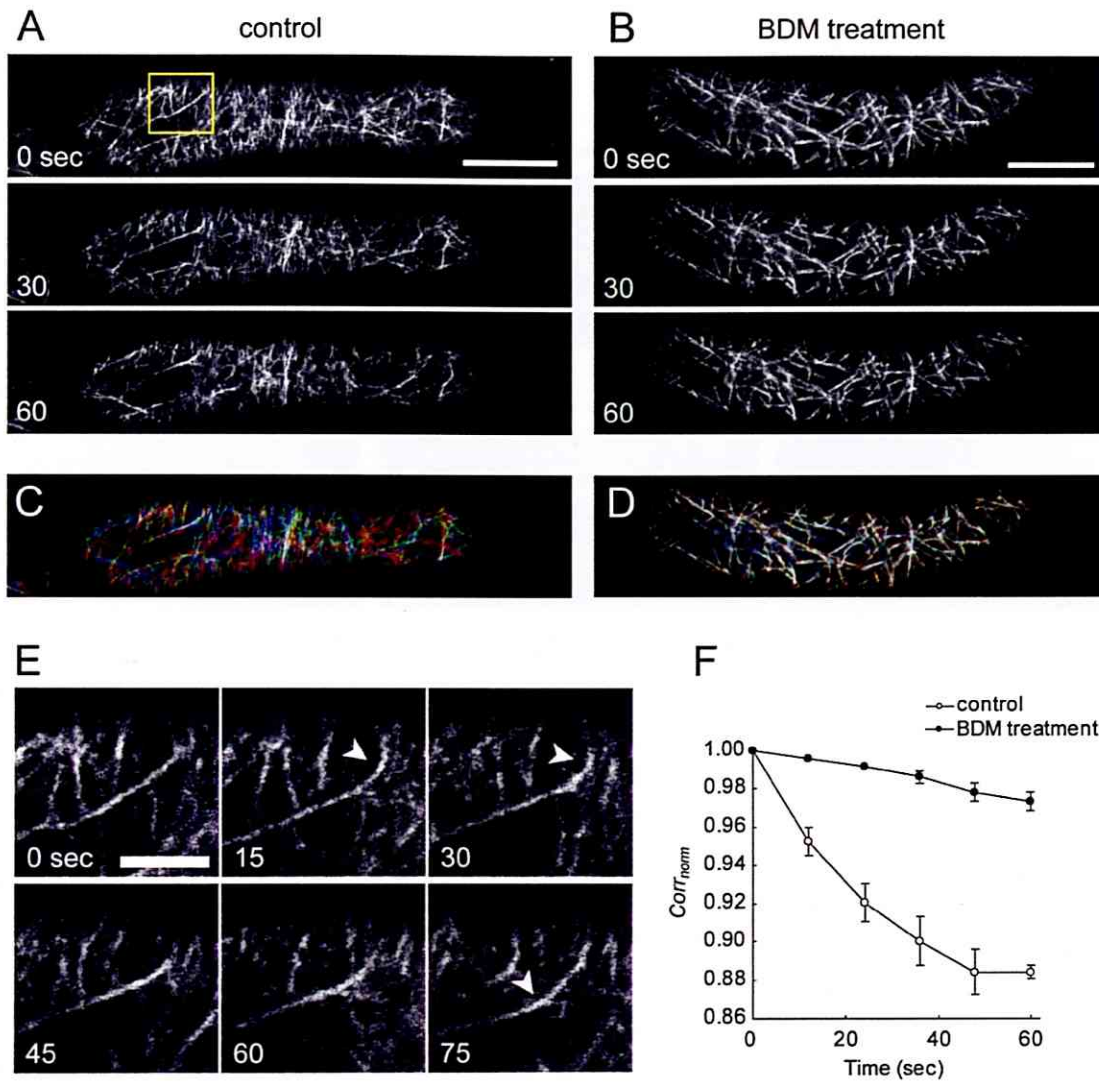


Figure III-5. Characterization of MF dynamics near the cell cortex. (A, B) Time-sequential image acquisition of cortical MFs was performed at 30 sec intervals for 60 sec in a single BY-GF11 cell (A) and in a BDM-treated BY-GF11 cell (B). BDM was applied 30 min before the observation. (C, D) Images at 0, 30 and 60 sec were colored red, green and blue, respectively, and projected together. White pixels represent static MFs and red/green/blue pixels represent dynamic MFs. Scale bar: 10 μ m. (E) Time-sequential images of the boxed region in (A) at 15 s intervals. Arrowheads show an MF which was constantly swinging. (F) Normalized correlation coefficient ($Corr_{norm}$) between the first image and the subsequent time-sequential images in control (open circle) and BDM-treated (filled circle) cells. Bars represent the standard error of three independent experiments.

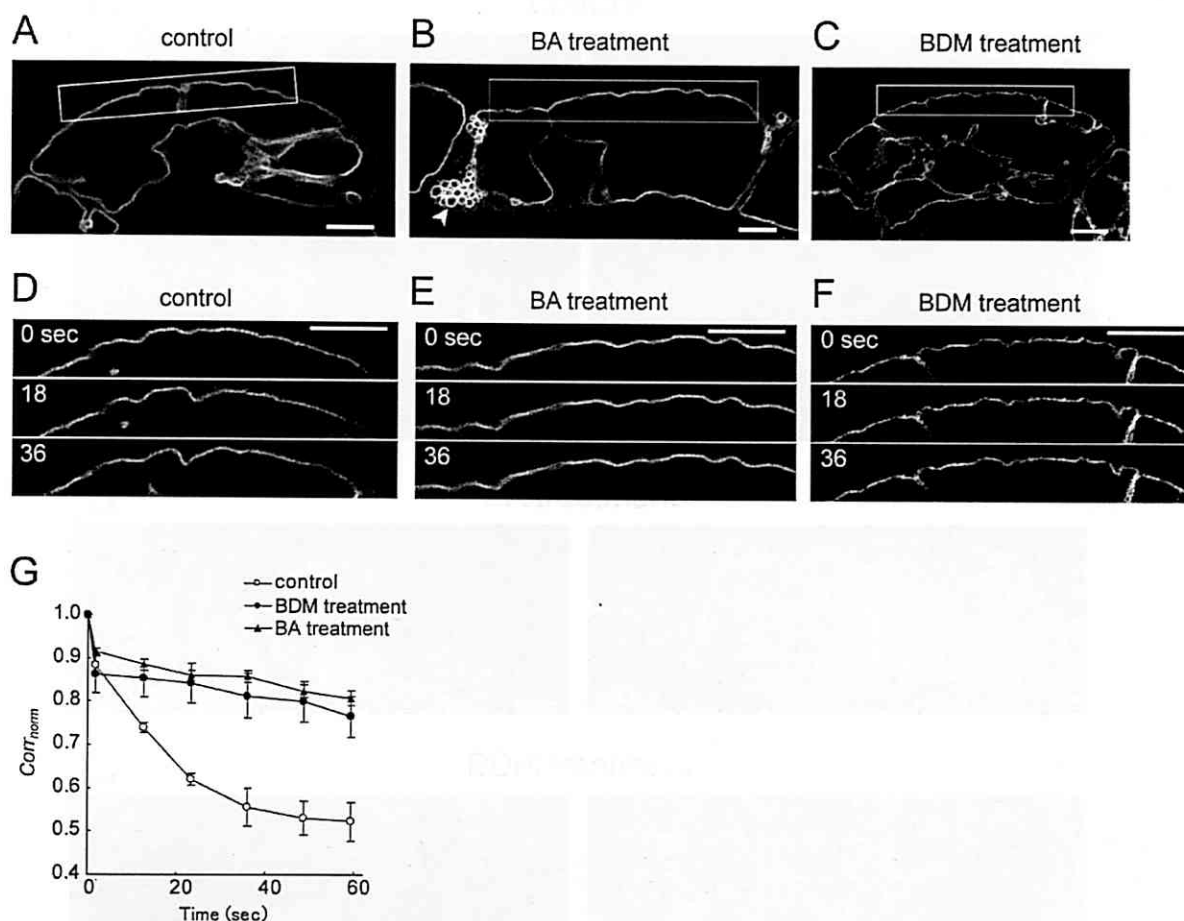


Figure III-6. Characterization of VM dynamics near the cell cortex in BY-GV7 cells. (A, B, C) Optical sections in the mid-plane of control (A), BA- (B) and BDM- (C) treated cells were captured by CLSM. BA or BDM was applied 1 hour or 30 min before the time-sequential observation, respectively. An arrowhead in (B) shows small spherical vacuoles. (D, E, F) Time-sequential images from the boxed regions shown in (A), (B) and (C) at 18 sec intervals were obtained. Scale bars: 10 μ m. (G) Normalized correlation coefficient ($Corr_{norm}$) between the first image and the subsequent time-sequential images in control (open circle), BDM-treated (filled circle) and BA-treated (filled triangle) cells. Bars represent the standard error of three independent experiments.

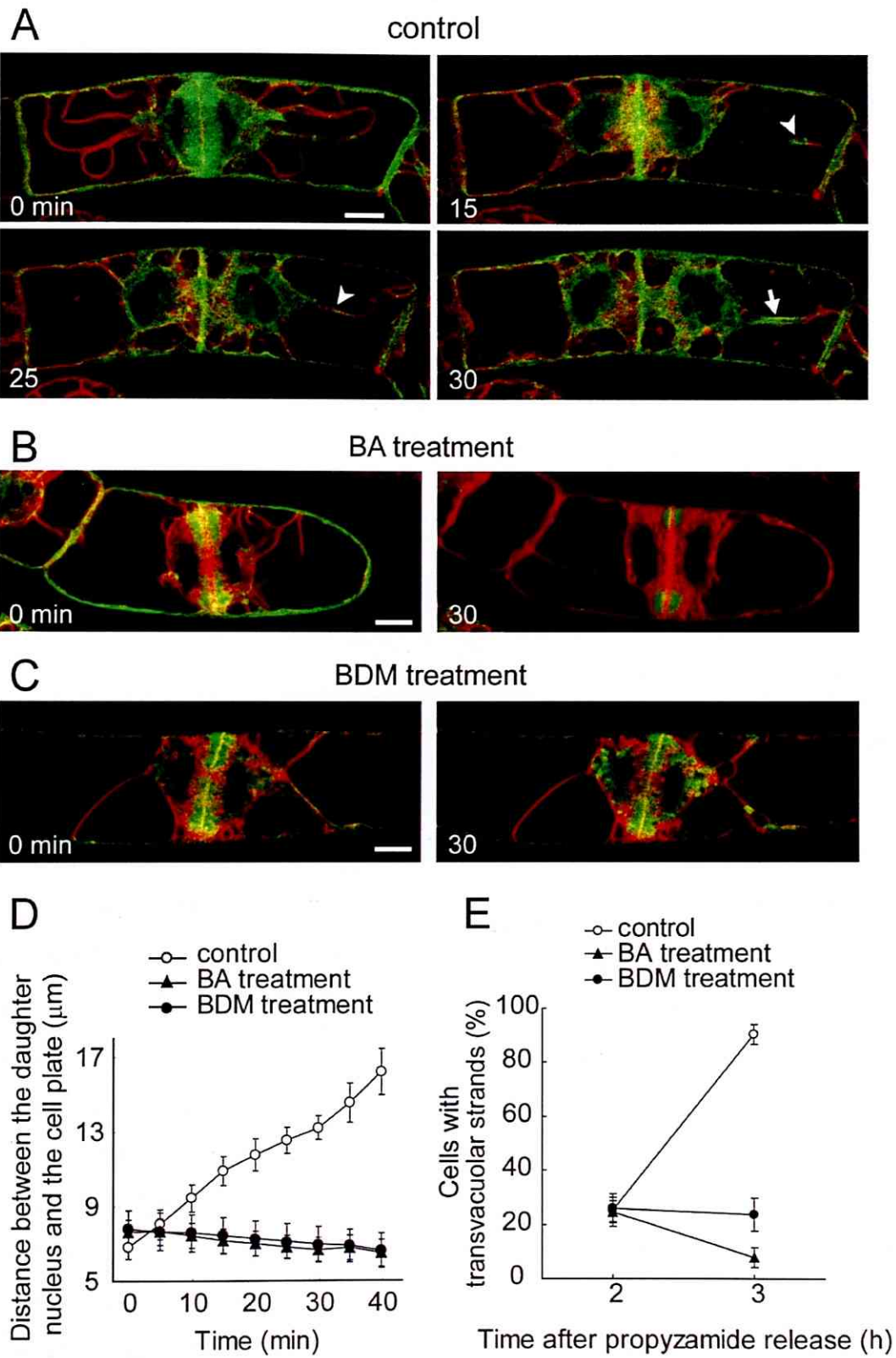


Figure III-7. Characterization of the reorganization of transvacuolar strands (TVSs) and migration of daughter cell nuclei at early G1 phase. (A) Time-sequential observations of MFs and VMs from late telophase (0 min) to early G1 phase (15-30 min). Green and red colors show GFP-ABD2 and FM4-64, respectively. Arrows show reorganized TVSs. (B) Effects of BA on vacuolar morphogenesis at early G1 phase. (C) Effects of BDM on vacuolar morphogenesis at early G1 phase. Scale bars: 10 μ m. (D) Changes of the distance between the daughter cell nuclei and the cell plate in early G1 phase in control (open circles), BA- (filled triangles) and BDM- (filled circles) treated cells. (E) Effects of BA and BDM on the reorganization of TVSs. BA or BDM was added 2 h after the release from propyzamide (M/G1 phase) in synchronized cells, and cells with TVSs were counted. Bars represent the standard error of three independent experiments.

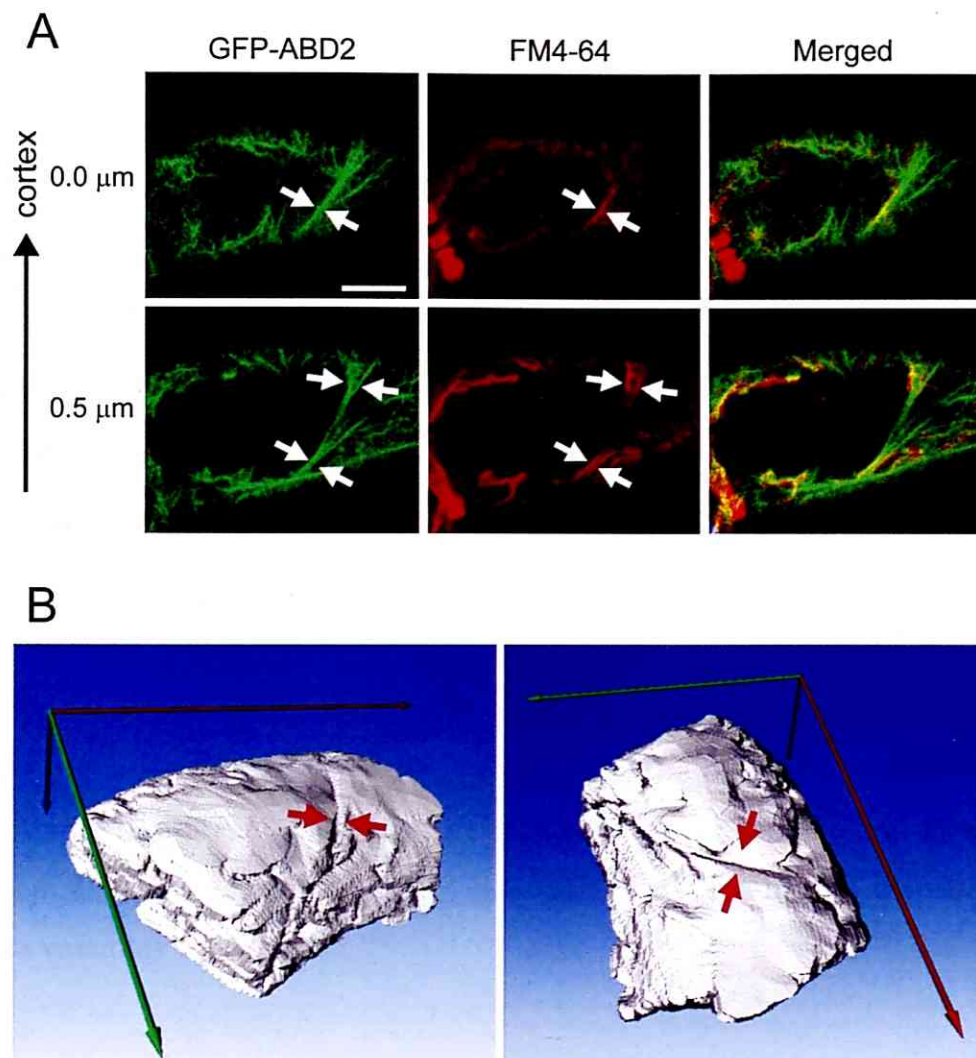


Figure III-8. Bundle-like structure of MFs and groove-like structure of the VM at early G1 phase. (A) A BY-GF11 cell at early G1 phase was observed by CLSM after GFP-ABD2 (green) and FM4-64 (red) treatment. Two focal planes near the cell cortex taken at 0.5 μm intervals. Arrows indicate the bundle-like structure of MFs close to the VM. Scale bars: 10 μm . (B) A 3-D images of vacuoles shown in (A). Red arrows indicate the groove-like structure of the VM.

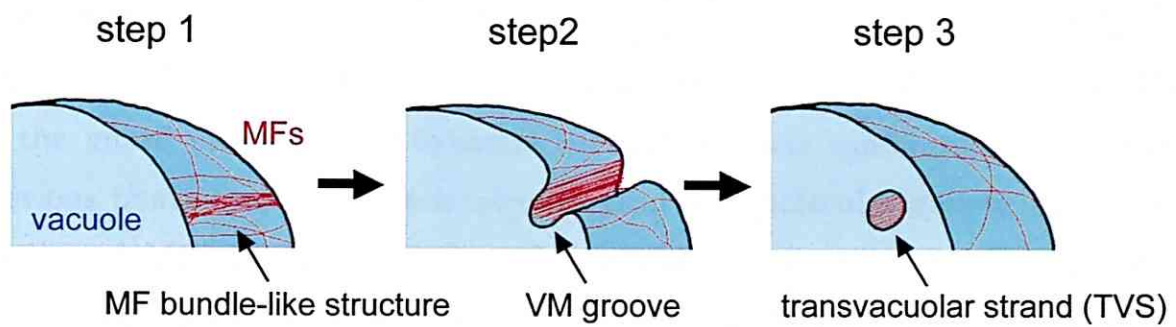


Figure III-9. Possible model of the reorganization of transvacuolar strands (TVSs) at early G1 phase. MFs accumulate and organize the bundle-like structures (step 1). The bundle-like structures invaginate into vacuolar lumen, and form the VM groove (step 2). The groove-like VM may fuse with itself and internalized the cytosol into vacuolar lumen (step 3).

Chapter IV: Stomatal movement

Abstract

Stomata, which consist of a pair of guard cells, open during the day and close at night in order to appropriately regulate gas and water vapor exchange between the plant and atmosphere. During stomatal movement, actin microfilaments (MFs) in the guard cells undergo dynamic changes in their configurations. Although previous pharmacological, electrophysiological and molecular genetic evidence has implicated MFs in the regulation of stomatal movement, it is unclear how the changes in MF configurations actually regulate such movement. In this chapter, using quantitative evaluation and cluster analysis of MF configurations from microscopic images, I determined that MFs are transiently bundled in the process of diurnal stomatal opening in *Arabidopsis thaliana*. In addition, continuous bundling induced by expression of GFP-mTn suppressed the diurnal patterns of stomatal opening. My results clearly illustrate that changes in the level of MF bundling are crucial for promoting stomatal movement.

Introduction

Stomata consist of a pair of symmetric guard cells and function as interfaces between a plant and the environment. They play roles as gates for gas and water exchange of the plants, and are regulated in response to changes in various environmental factors, such as light and humidity. Stomatal movement originates from changes in turgor pressure of the guard cells, which is under control of the mechanics of the cell wall of guard cells. That is, stomata open when the guard cell volumes increase and close when the cell volumes decrease.

The involvement of actin microfilaments (MFs) in stomatal movement has been demonstrated by various pharmacological studies. For example, the actin inhibitor, cytochalasin D (CD), has been shown to promote light-induced stomatal opening (Kim et al. 1995, Liu and Lian, 1998), whereas the actin inhibitor, latrunculin B (LatB), promotes abscisic acid (ABA)-induced stomatal closure (MacRobbie and Kurup 2007). The actin stabilizers, phalloidin and jasplakinolide (JK), inhibit ABA-induced stomatal closing (Kim et al. 1995, MacRobbie and Kurup 2007), but whereas phalloidin also inhibits light-induced stomatal opening (Kim et al. 1995), JK has no effect on the stomatal opening (MacRobbie and Kurup 2007). Furthermore, molecular genetic approaches have revealed that stomatal closure and MF disruption can be co-induced by either inactivation of the small GTPase, AtRac1 (Lemichez et al. 2001), or by overexpression of the actin depolymerization factor, AtADF1 (Dong et al. 2001).

Although the precise roles of MFs in stomatal movement are still unclear, electrophysiological studies have suggested that they affect ion homeostasis in response to osmotic conditions via regulation of ion channel activities. For example, CD promotes potassium influx in guard cell protoplasts under hyperosmotic conditions but has no such effect in hypoosmotic conditions (Hwang et al. 1997, Liu and Lian 1998). Furthermore, hypoosmotic stress has been shown to induce MF disruption in guard cell protoplasts (Liu and Lian 1998). Based on a series of observations, a potassium channel-based positive feedback model was proposed (Liu

and Lian 1998, reviewed by Galatis and Apostolakos 2004) in which MFs function as osmosensors, by self-disruption in response to guard cell swelling, so that potassium influx is consequently promoted and stomatal opening accelerated. Stretch-activated calcium channels that are activated by MF disruption have been proposed as a brake of the positive feedback mechanism (Zhang et al. 2007a). The possible regulation of potassium channels by MFs has also been suggested in tobacco BY-2 cells (Stoeckel and Takeda 2002) and bean seed coat cells (Zhang et al. 2007b). On the other hand, visualization of MFs by rhodamine-phalloidin staining or GFP-mouse talin (mTn) expression has shown that MFs are not disrupted but form a radial orientation in guard cells of open stomata (Kim et al. 1995, Hwang and Lee 2001, Lemichez et al. 2001, Choi et al. 2008, Gao et al. 2008). Thus, a unified concept of MF dynamics and their roles in stomatal movement is lacking at present.

In this chapter, I quantitatively evaluated MF dynamics during diurnal stomatal movement by microscopic image analysis techniques, and determined that the levels of actin bundling in guard cells regulate stomatal apertures. These results provide the basis for a unified hypothetical model of MF dynamics and their roles in stomatal movement.

Methods

Construction of GFP-ABD2 and in planta transformation

Construction of GFP-ABD2 has been performed as described in chapter I (Sano and Higaki et al. 2005). The pCAMBIA1300 binary vector (CAMBIA, Canberra, Australia) including GFP-ABD2 construct was introduced into *Agrobacterium tumefaciens* (strain LBA4404) by electroporation. *Arabidopsis* (*Arabidopsis thaliana* ecotype Columbia) was infected with the *A. tumefaciens* by *in planta* transformation and grown in Murashige-Skoog medium containing hygromycin (25 µg/mL). Transgenic plants expressing GFP-ABD2 were selected under a conventional fluorescence microscope.

Plant materials and growth conditions

Seeds of transgenic *Arabidopsis* expressing GFP-mTn were kindly provided by Drs Miyo Terao-Morita and Masao Tasaka (Saito et al. 2005). *Arabidopsis* plants were grown on soil-vermiculite, as described by Naito et al. (1994), in growth chambers at 23.5 °C, a 60% relative humidity, and a 12/12-hour light/dark cycle using 100 $\mu\text{mol m}^{-2}\text{s}^{-1}$ white lights. Fully expanded rosette leaves of 4- to 5-week-old plants were used for experiments.

Microscopic image acquisition

To capture image of the stomatal MFs, epidermal strips were transferred onto a slide glass and covered by a coverglass (Matsunami, Osaka, Japan). The slide glass was placed onto the inverted platform of a fluorescence microscope (IX70, Olympus) equipped with an UplanApo 100x/1.35 oil iris objective lens and a CSU10 scanning head (Yokogawa, Tokyo, Japan) together with a cooled CCD camera head system (CoolSNAP HQ, PhotoMetrics). At image acquisition, all settings including laser strength (20 mW, wavelength 488 nm argon laser from HPU-50101-PFS2, Furukawa, Tokyo, Japan), emission filter (collection between 524 and 546 nm by FF01-535/22-25, Semrock, Rochester, NY, USA), pixel width (0.064 μm) and step size for 3-D imaging (0.5 μm) were fixed.

Microscopic image evaluation and classification

To evaluate the MF orientations, I measured the mean angular difference between MF pixel pairs and the nearest pixel pairs of the stomatal pore edges in the processed images for the calculation (Fig. IV-S2A, B, C, D, E). The mean angular difference $\Delta\theta$ is defined by

$$\Delta\theta = \frac{1}{N} \sum_{i=1}^N \arcsin|\sin(\theta_{MF} - \theta_{StEdge})|$$

where N , θ_{MF} and θ_{StEdge} are the number of MF pixel pairs, angles of MF pixel pairs, and pixel pairs of the nearest stomatal pore edge, respectively. θ_{MF} and θ_{StEdge} are discretized into 0, 45, 90 and 135° (Fig. IV-S2F).

To preprocess the quantitative evaluations of MF bundling and density, the serial optical sections of the guard cell MF images were skeletonized, projected and masked by manually segmenting the cell region images (Fig. IV-S5). To estimate MF bundling, I used the skewness of intensity distribution of the MF pixels as an indicator of MF bundling. The skewness is defined by

$$skewness = \frac{1}{N} \sum_{i=1}^N \left(\frac{i_n - \bar{i}}{\sigma} \right)^3$$

$$\sigma = \frac{1}{N} \sum_{i=1}^N (i_n - \bar{i})^2$$

where N , i_n and \bar{i} are the MF pixel numbers, intensity of an MF pixel, and the mean intensity of MF pixels, respectively. As the GFP-fluorescence intensity in the pixels increase by MF bundling, the skewness becomes higher (Fig. IV-S3).

To estimate the MF density, I defined the occupancy of the GFP signal calculated from the skeletonized image and guard cell region image (Fig. IV-S4). The occupancy is defined by

$$occupancy = 100 \cdot \frac{n_{MF}}{n_{Cell}}$$

where n_{MF} and n_{Cell} are the pixel numbers constituting the skeletonized MFs and cell region. The occupancy becomes lower as the MFs are depolymerized or fragmented (Fig. IV-S4).

All procedures were performed using the Java plug-ins and macros; SignalSkewness, ThinLine and StomataRadial on ImageJ (Abramoff et al. 2004). These plug-ins and macros were developed by Dr. Natusmaro Kustuna (The University of Tokyo) and myself, respectively. These programs are available from Kashiwa BioImaging website (<http://hasezawa.ib.k.u-tokyo.ac.jp/zp/Kbi>).

For image classification, the data were classified into groups through a hierarchical cluster analysis using Minitab software (Minitab Inc., State College, PA, USA).

Results

Establishment of transgenic Arabidopsis expressing GFP-ABD2 and image acquisition of guard cell MFs

As a marker of MFs, I expressed GFP fusions to a second actin-binding domain (ABD2) of the AtFIM1 protein (GFP-ABD2) fusion construct (chapter I, Sano and Higaki et al. 2005) in *Arabidopsis* plants, and observed three lines (GF1-3, GF1-7, GF3-1) homozygous for the transgene that were established from independent T2 lines. The three GFP-ABD2 expression lines showed basically indistinguishable MF configurations in their guard cells as well as normal diurnal stomatal movements compared with untransformed plants (Fig. IV-S1).

To study diurnal changes in the MF configurations, I first observed MFs in guard cells sampled from plants, grown under 12-h (7:00 hours-19:00 hours)-light/12-h (19:00 hours-7:00 hours)-dark cycles, at different times of the day. Figure IV-1 shows representative images of MF configurations at 6:00 hours (Fig. IV-1A), 12:00 hours (Fig. IV-1B), 18:00 hours (Fig. IV-1C) and 0:00 hours (Fig. IV-1D). The stomatal MFs appeared to be drastically altered, but not completely disrupted, during the diurnal cycles (Fig. IV-1). I therefore attempted to quantify the MF configurations by 3-D and statistical analysis of 0.5 μm -interval serial optical sections of GFP-ABD2-labelled MFs in 38-45 pairs of guard cells at 2-hour intervals during the diurnal cycle. Thereafter, I measured stomatal apertures and the three metric parameters from 492 guard cell MFs images using the image analysis techniques described below.

Numeric evaluation of guard cell MF configuration using image analysis techniques

To quantitatively examine the MF configurations, I developed three new metric parameters: (1) the mean angular difference between MF pixel pairs and the nearest pixel pairs of stomatal pore edges as a metric of MF orientation, (2) the skewness of an intensity histogram as a metric of MF bundling, and (3) occupancy of the GFP-signal as a metric of MF density. To evaluate the MF orientations, I

measured the mean angular differences in the skeletonized MF and segmented stomatal pore region images (Fig. IV-S2; see also Methods for the definition). This mean angular difference has the highest value, 90°, when MFs have a perfect radial orientation and the lowest value, 0°, when MFs have a perfect longitudinal orientation. A random orientation was detected as a mean angular difference of around 45°. To evaluate the extent of MF bundling, I measured the skewness of the fluorescence intensity distribution in skeletonized images (see Methods for the definition). Skewness is a measure of the degree of asymmetry of a distribution, and the value becomes higher when high fluorescence intensity pixels numbers increase by MF bundling (Fig. IV-S3). To evaluate MF density, I defined the GFP signal occupancy that is an indicator of the proportion of pixel numbers constituting the skeletonized MFs of the total pixel numbers constituting the cell region (see Methods for definition). The occupancy becomes lower when the MFs are depolymerized or fragmented (Fig. IV-S4).

Using these image analysis methods, I examined the relationship between stomatal aperture and the three metric parameters of MF configurations (Fig. IV-2A, B, C), and found that stomatal aperture has a strong positive correlation with MF orientation but not with bundling or density (Fig. IV-2A). Time-averaged values also clearly showed a strong correlation between stomatal aperture and MF orientation (Pearson correlation coefficient = +0.90, Fig. IV-2D), with MFs being radially oriented in guard cells of open stomata, and longitudinally oriented in guard cells of closed stomata. In addition, I found that MF bundling increased at the initial phase of stomatal opening (Fig. IV-2E, 8:00 hours), whereas MF density increased at the close/open and open/close transition phases (Fig. IV-2F, 2:00 and 18:00 hours).

Cooperative changes in MF configuration with diurnal rhythm: classification of MF configurations by clustering of microscopic images

Since the evaluation of MF configurations presented above were deduced from the mean values of multiple guard cells, they could not adequately describe the

organization of MFs in individual pairs of guard cells. Therefore, to examine the MF changes in individual stomatal guard cells, I attempted to quantitatively classify the microscopic images (492 pairs of guard cells with diurnal cycles) by cluster analysis based on the three MF metric patterns. I observed a weak correlation among the three metric parameters (Pearson correlation coefficient = -0.16, +0.07 and -0.17 in mean angular difference *vs.* occupancy, mean angular difference *vs.* skewness, and skewness *vs.* occupancy, respectively), suggesting that these parameters are applicable to cluster analysis. As a result, all the images could be classified into four classes; class 1 (28.9%, highlighted by orange in Fig. IV-3A), class 2 (26.6%, highlighted by red in Fig. IV-3A), class 3 (22.6%, highlighted by blue in Fig. IV-3A) and class 4 (21.9%, highlighted by green in Fig. IV-3A). Mean values of the metrics and representative images in each class are shown in Table IV-1 and Figure IV-3B-E, respectively. I termed class 1 MFs as “radial bundles” because of their radial orientation with the highest bundling level; class 2 as “radial arrays” because of their radial orientation; class 3 as “longitudinal arrays” because of their lowest mean angular differences; and class 4 as “random meshworks” because of their random orientation and highest density. Furthermore, the 3-D visualization of these characteristics of the MF configurations in each class, using Modrec software (Kutsuna et al., unpublished; available from Kahiswa BioImaging website: <http://hasezawa.ib.k.u-tokyo.ac.jp/zp/Kbi/ModrecProj>), confirms the utility of my dimension reduction approach by maximum intensity projection (Fig. IV-3F, G, H, I). When I examined the relationship between stomatal apertures and the appearance frequency of each class, I found that the longitudinal arrays tended to appear in closed stomata (Fig. IV-4A), while the radial bundles and radial arrays were more prominent in open stomata (Fig. IV-4C, D). Time-series data also indicated that the longitudinal arrays appeared in closed stomata during the dark periods (Fig. IV-4E). Interestingly, I also observed that radial bundles were most prominent at 8:00 hours (1 hour after the start of the light period), which is the initiation phase of stomatal opening (Fig. IV-4G), whereas the radial arrays were prominent at 10:00 hours when most of the stomata had opened (Fig. IV-4H). These results suggest that MFs were

transiently bundled in the process of stomatal opening.

Comparative analysis of GFP-ABD2 and GFP-mTn expression lines

To examine the physiological impact of actin bundling, I subsequently performed similar experiments using GFP-mTn expression lines. GFP-mTn is a popular and useful MF probe (Kost et al. 1998, Saito et al. 2005), however, it is generally accepted that it may induce extra bundling of MFs (Sheahan et al. 2004, Ketelaar et al. 2004, Maisch and Nick 2007). As with the GFP-ABD2 expressing lines, I performed image acquisition of stomatal MFs during the diurnal cycles and measured the three metric parameters as indicators of MF orientation, bundling and density (Fig. IV-S6). Interestingly, in comparison with the GFP-ABD2-expressing lines, stomatal opening and radial patterning of the MFs was suppressed (Fig. IV-5A, B) while, as expected, MF bundling was enhanced during the diurnal cycles (Fig. IV-5C). Furthermore, the diurnal rhythms of MF density were perturbed (Fig. IV-5D).

Cluster analysis enabled the 529 GFP-mTn images to be classified into four classes (Fig. IV-6A); class 1 (36.9%, highlighted by blue in Fig. IV-6A), class 2 (29.5%, highlighted by green in Fig. IV-6A), class 3 (23.8%, highlighted by red in Fig. IV-6A), and class 4 (9.8%, highlighted by orange in Fig. IV-6A). Based on the mean values of the MF configuration indicators (Table IV-1), these classes are referred to as “longitudinal bundles” (Fig. IV-6B), “longitudinal bundle-meshworks” (Fig. IV-6C), “random bundles” (Fig. IV-6D) and “longitudinal heavy-bundles” (Fig. IV-6E), respectively. The characteristics of the MF configurations in each class were confirmed by 3-D modeling (Fig. IV-6F, G, H, I). The relationship between stomatal apertures and each class indicated that random bundles and longitudinal heavy-bundles (Fig. IV-7C, D) were more prominent than other classes (Fig. IV-7A, B) in relatively open stomata. Time-series data also showed that random bundles appeared during the light period (Fig. IV-7G), suggesting that the GFP-mTn-labelled MFs stopped short of radial orientation in situations of suppressed stomatal opening. In addition, the longitudinal heavy-bundles were present continuously during the

light period (Fig. IV-7H), suggesting that the MF bundling level increased after lightening, as in the GFP-ABD2 expressing line, although the dissolution of MF bundles was perturbed by GFP-mTn.

Discussion

In this study, I acquired microscopic images of MFs labeled by GFP-ABD2 or GFP-mTn during the diurnal cycle of *Arabidopsis* guard cells. From the images, I quantitatively estimated the changes in MF configurations, including MF orientation, bundling and density using my original image analysis system, and consequently identified the dynamic changes in actin bundling levels during stomatal opening. I also observed that GFP-mTn-induced excess bundling impaired stomatal opening. Based on these series of observations, I propose a regulatory mechanism of stomatal movement by the actin bundling levels.

Quantification and classification of cytoskeletal structures

In cell biological studies, the evaluation and classification of the cell status is primarily based on qualitative assessments by researchers, even though such approaches possess considerable risk of error especially when large amounts of image data need to be analyzed. In this study, I formulated new metric parameters that serve as indicators of the MF configurations and quantitatively evaluated them from microscopic images obtained throughout the diurnal cycle. My methodology is useful for quantitatively estimating the cytoskeletal structures in any cell type, as previously shown for microtubule and cellulose microfibril orientations in tobacco BY-2 protoplasts (Yoneda et al. 2007). In addition, quantitative data for the cytoskeletal configurations together with cluster analysis allowed me to objectively classify the MF configurations. Cluster analysis of microscopic images has recently been applied for classification of sub-cellular localizations (Hamilton and Teasdale 2008), and also appears to be useful for cell classification based on intracellular architectures as shown in this study. My results are basically consistent with

previous concepts of MF configurations, especially in that they have a radial orientation in open stomata and a longitudinal orientation in closed stomata, as derived from qualitative evaluations of MF configurations in guard cells of *Commelina communis* and *Arabidopsis thaliana* (Hwang and Lee 2001, Lemichez et al. 2001). These findings are indicative of the validity of my approach.

Predicted roles of transient MF bundling in stomatal opening

I established that MFs were transiently bundled in the process of stomatal opening (Figs IV-2E, 4G; 8:00 hours) and that the bundles dissolved when stomatal opening completed (Figs IV-2E, 4H; 10:00 hours). In the GFP-mTn expressing lines, the heavy-bundles appeared continuously during the light period and stomatal opening was suppressed (Fig. IV-7H). These results suggest that the formation of MF bundles and their dissolution promote stomatal opening.

To explain the roles of MFs in stomatal movement, Liu and Luan (1998) proposed the potassium-channel-based positive feed-back model in which an increase in turgor pressure during stomatal opening causes disruption of the MFs and consequently activates voltage-gated potassium channels in the plasma membrane so that the guard cells acquire increased turgor pressure. This model is mainly based on the observation that the actin polymerization inhibitor, CD, promotes the potassium channel activities in guard cell protoplasts, and that the resulting hypoosmotic stress induces MF disruption (Liu and Luan 1998). Although this experimental observation is supported by pharmacological studies in different experimental systems (Kim et al. 1995, Hwang et al. 1997, MacRobbie and Kurup 2007), immunostaining and live imaging of MFs also demonstrated the existence of intact MFs in guard cells of open stomata (Kim et al. 1995, Eun and Lee 1997, Hwang and Lee 2001, Lemichez et al. 2001, Choi et al. 2008, Gao et al. 2008, this study). Therefore, taken together with my results from this study, I infer that dissolution of the MF bundles, rather than MF disruption, enhances stomatal opening via activation of potassium channels as described in Figure IV-8. As CD occasionally induces a reduction in the MF bundles (Williamson & Hurley 1986) that

may mimic their dissolution, my hypothetic model does not contradict previous results. Interestingly, in the seismonastic movements of *Mimosa pudica*, it has been shown that the MF bundles become looser after bending (Kanzawa et al. 2006), suggesting the universal importance of MF dissolution in regulating turgor movement.

Two possible mechanisms can be hypothesized to explain how the dissolution of actin bundles induces activation of potassium channels in guard cells. One possible mechanism is through the modulation of potassium channel activity by the dissolved MFs. In animal cells, MFs have been proposed to directly interact and modulate ion channels, including sodium (Berdiev et al. 1996, Jovov et al. 1999, Mazzochi et al. 2006), chloride (Ahmed et al. 2000) and potassium (Grunnet et al. 2003) channels. Therefore, the dissolved MFs may actually attach to the channels in guard cells and modulate their activity, and this is supported by the radially-stripped localization pattern of a potassium channel KAT1-GFP fusion (Homann et al. 2007) that resembles the radial pattern of dissolved MFs in guard cells of open stomata. The other possible mechanism of potassium channel activation in guard cells is through trafficking of the channels. The involvement of MFs in the translocation of water channel aquaporins between the plasma membrane and endocytic vesicles in animal cells is well documented (Klussmann et al. 2001, Tajika et al. 2005, Noda and Sasaki 2006). In plant guard cells, KAT1 localizes to both the plasma membrane and endosomes (Hurst et al. 2004, Meckel et al. 2004), indicative of the importance of membrane trafficking in guard cell ion homeostasis. The attachment of MFs to endosomes was observed in root hair cells and cytokinetic BY-2 cells (Voigt et al. 2005, chapter II, Higaki et al. 2008), while Myosin VIII also colocalized to endosomes in root and leaf cells (Golomb et al. 2008). These results suggest an actin-based mechanism of endosome movement in plants. In this context, a recent study has revealed that auxin transport inhibitors induce MF bundling and that the inhibitor-induced MF bundles impair endosome movement (Dhonukshe et al. 2008). Taken together with these results, it is possible that MF dissolution stimulates membrane trafficking and increases the number of

activated potassium channels in the plasma membrane of guard cells. Future studies on the co-localization of MFs and channels and their dynamics will clarify the mechanism of MF dissolution-driven promotion of stomatal movement.

References

- Abramoff MD, Magelhaes PJ, Ram SJ. (2004) Image processing with ImageJ. *Biophoto. Int.* 11:36-42.
- Ahmed N, Ramjeesingh M, Wong S, Varga A, Garami E, Bear CE. (2000) Chloride channel activity of ClC-2 is modified by the actin cytoskeleton. *Biochem. J.* 352: 789-794.
- Berdiev BK, Prat AG, Cantiello HF, Ausiello DA, Fuller CM, Jovov B, Benos DJ, Ismailov II. (1996) Regulation of epithelial sodium channels by short actin filaments. *J. Biol. Chem.* 271:17704-17710.
- Choi Y, Lee Y, Jeon BW, Staiger CJ, Lee Y. (2008) Phosphatidylinositol 3- and 4-phosphate modulate actin filament reorganization in guard cells of day flower. *Plant Cell Environ.* 31:366-377.
- Dhonukshe P, Grigoriev I, Fischer R, Tominaga M, Robinson DG, Hasek J, Paciorek T, Petrasek J, Seifertova D, Tejos R, Meisel LA, Zazimalová E, Gadella TW Jr, Stierhof YD, Ueda T, Oiwa K, Akhmanova A, Brock R, Spang A, Friml J. (2008) Auxin transport inhibitors impair vesicle motility and actin cytoskeleton dynamics in diverse eukaryotes. *Proc. Natl. Acad. Sci. U. S. A.* 105:4489-4494.
- Dong CH, Xia GX, Hong Y, Ramachandran S, Kost B, Chua NH. (2001) ADF proteins are involved in the control of flowering and regulate F-actin organization, cell expansion, and organ growth in *Arabidopsis*. *Plant Cell* 13:1333-1346.
- Eun SO, Lee Y (1997) Actin filaments of guard cells are reorganized in response to light and abscisic acid. *Plant Physiol.* 115:1491-1498.
- Gao XQ, Chen J, Wei PC, Ren F, Chen J, Wang XC. (2008) Array and distribution of actin filaments in guard cells contribute to the determination of stomatal aperture. *Plant Cell Rep.* 27:1655-1665.
- Galatis B, Apostolakis P. (2004) The role of the cytoskeleton in the morphogenesis and function of stomatal complexes. *New Phytol.* 161:613-639.
- Golomb L, Abu-Abied M, Belausov E, Sadot E. (2008) Different subcellular localizations and functions of *Arabidopsis* myosin VIII. *BMC Plant Biol.* 8:3.

- Grunnet M, Jespersen T, MacAulay N, Jorgensen NK, Schmitt N, Pongs O, Olesen SP, Klaerke DA. (2003) KCNQ1 channels sense small changes in cell volume. *J. Physiol.* 549:419-427.
- Hamilton NA, Teasdale RD. (2008) Visualizing and clustering high throughput sub-cellular localization imaging. *BMC Bioinformatics* 9:81.
- Higaki T, Kutsuna N, Sano T, Hasezawa S. (2008) Quantitative analysis of changes in actin microfilament contribution to cell plate development in plant cytokinesis. *BMC Plant Biol.* 8:80.
- Homann U, Meckel T, Hewing J, Hutt MT, Hurst AC. (2007) Distinct fluorescent pattern of KAT1::GFP in the plasma membrane of *Vicia faba* guard cells. *Eur. J. Cell Biol.* 86:489-500.
- Hurst AC, Meckel T, Tayefeh S, Thiel G, Homann U. (2004) Trafficking of the plant potassium inward rectifier KAT1 in guard cell protoplasts of *Vicia faba*. *Plant J.* 37:391-397.
- Hwang JU, Suh S, Yi H, Kim J, Lee Y. (1997) Actin filaments modulate both stomatal opening and inward K⁺-channel activities in guard cells of *Vicia faba* L. *Plant Physiol.* 115:335-342.
- Hwang JU, Lee Y. (2001) Absciscic acid-induced actin reorganization in guard cells of dayflower is mediated by cytosolic calcium levels and by protein kinase and protein phosphatase activities. *Plant Physiol.* 125:2120-2128.
- Jovov B, Tousson A, Ji HL, Keeton D, Shlyonsky V, Ripol, PJ, Fuller CM, Benos DJ. (1999) Regulation of epithelial Na⁺ channels by actin in planar lipid bilayers and in the *Xenopus* oocyte expression system. *J. Biol. Chem.* 274:37845-37854.
- Kanzawa N, Hoshino Y, Chiba M, Hoshino D, Kobayashi H, Kamasawa N, Kishi Y, Osumi M, Sameshima M, Tsuchiya T. (2006) Change in the actin cytoskeleton during seismonastic movement of *Mimosa pudica*. *Plant Cell Physiol.* 47:531-539.
- Ketelaar T, Anthony RG, Hussey PJ. (2004) Green fluorescent protein-mTalin causes defects in actin organization and cell expansion in *Arabidopsis* and inhibits actin depolymerizing factor's actin depolymerizing activity *in vitro*. *Plant Physiol.* 136:3990-3998.

- Kim M, Hepler PK, Eun SO, Ha KS, Lee Y. (1995) Actin filaments in mature guard cells are radially distributed and involved in stomatal movement. *Plant Physiol.* 109:1077-1084.
- Klussmann E, Tamma G, Lorenz D, Wiesner B, Maric K, Hofmann F, Aktories K, Valenti G, Rosenthal W. (2001) An inhibitory role of Rho in the vasopressin-mediated translocation of aquaporin-2 into cell membranes of renal principal cells. *J. Biol. Chem.* 276:20451-20457.
- Kost B, Spielhofer P, Chua NH. (1998) A GFP-mouse talin fusion protein labels plant actin filaments *in vivo* and visualizes the actin cytoskeleton in growing pollen tubes. *Plant J.* 16:393-401.
- Lemichez E, Wu Y, Sanchez JP, Mettouchi A, Mathur J, Chua NH. (2001) Inactivation of AtRac1 by abscisic acid is essential for stomatal closure. *Genes Dev.* 15:1808-1816.
- Liu K, Luan S. (1998) Voltage-dependent K⁺ channels as targets of osmosensing in guard cells. *Plant Cell* 10:1957-1970.
- Noda Y, Sasaki S. (2006) Regulation of aquaporin-2 trafficking and its binding protein complex. *Biochim. Biophys. Acta -Biomembranes* 1758:1117-1125.
- MacRobbie EA, Kurup S. (2007) Signalling mechanisms in the regulation of vacuolar ion release in guard cells. *New Phytol.* 175:630-640.
- Maisch J, Nick P. (2007) Actin is involved in auxin-dependent patterning. *Plant Physiol.* 143:1695-1704.
- Mazzochi C, Bubien JK, Smith PR, Benos DJ. (2006) The carboxyl terminus of the alpha-subunit of the amiloride-sensitive epithelial sodium channel binds to F-actin. *J. Biol. Chem.* 281:6528-6538.
- Meckel T, Hurst AC, Thiel G, Homann U. (2004) Endocytosis against high turgor: intact guard cells of *Vicia faba* constitutively endocytose fluorescently labelled plasma membrane and GFP-tagged K-channel KAT1. *Plant J.* 39:182-193.
- Naito S, Hirai MY, Chino M, Komeda Y. (1994) Expression of a soybean (*Glycine max* [L.] Merr.) seed storage protein gene in transgenic *Arabidopsis thaliana* and its response to nutritional stress and to abscisic acid mutations. *Plant Physiol.*

104:497-503.

- Saito C, Morita MT, Kato T, Tasaka M. (2005) Amyloplasts and vacuolar membrane dynamics in the living graviperceptive cell of the *Arabidopsis* inflorescence stem. *Plant Cell* 17:548-558.
- Sano T, Higaki T, Oda Y, Hayashi T, Hasezawa S (2005) Appearance of actin microfilament 'twin peaks' in mitosis and their function in cell plate formation, as visualized in tobacco BY-2 cells expressing GFP-fimbrin. *Plant J.* 44:595-605.
- Sheahan MB, Staiger CJ, Rose RJ, McCurdy DW. (2004) A green fluorescent protein fusion to actin-binding domain 2 of *Arabidopsis* fimbrin highlights new features of a dynamic actin cytoskeleton in live plant cells. *Plant Physiol.* 136:3968-3978.
- Stoeckel H, Takeda K. (2002) Plasmalemmal voltage-activated K⁺ currents in protoplasts from tobacco BY-2 cells: possible regulation by actin microfilaments? *Protoplasma* 220:79-87.
- Tajika Y, Matsuzaki T, Suzuki T, Ablimit A, Aoki T, Hagiwara H, Kuwahara M, Sasaki S, Takata K. (2005) Differential regulation of AQP2 trafficking in endosomes by microtubules and actin filaments. *Histochem. Cell Biol.* 124:1-12.
- Voigt B, Timmers AC, Samaj J, Hlavacka A, Ueda T, Preuss M, Nielsen E, Mathur J, Emans N, Stenmark H, Nakano A, Baluska F, Menzel D. (2005) Actin-based motility of endosomes is linked to the polar tip growth of root hairs. *Eur. J. Cell Biol.* 84:609-621.
- Williamson RE, Hurley UA. (1986) Growth and regrowth of actin bundles in *Chara*: bundle assembly by mechanisms differing in sensitivity to cytochalasin. *J. Cell Sci.* 85:21-32.
- Yoneda A, Higaki T, Kutsuna N, Kondo Y, Osada H, Hasezawa S, Matsui M. (2007) Chemical genetic screening identifies a novel inhibitor of parallel alignment of cortical microtubules and cellulose microfibrils. *Plant Cell Physiol.* 48:1393-1403.
- Zhang W, Fan LM, Wu WH. (2007a) Osmo-sensitive and stretch-activated calcium-permeable channels in *Vicia faba* guard cells are regulated by actin dynamics. *Plant Physiol.* 143:1140-1151.
- Zhang WH, Partick JW, Tyerman SD. (2007b) Actin filaments modulate

hypoosmotic-responsive K⁺ efflux channels in specialized cells of developing bean seed coats. *Funct. Plant Biol.* 34:874-884.

Figures

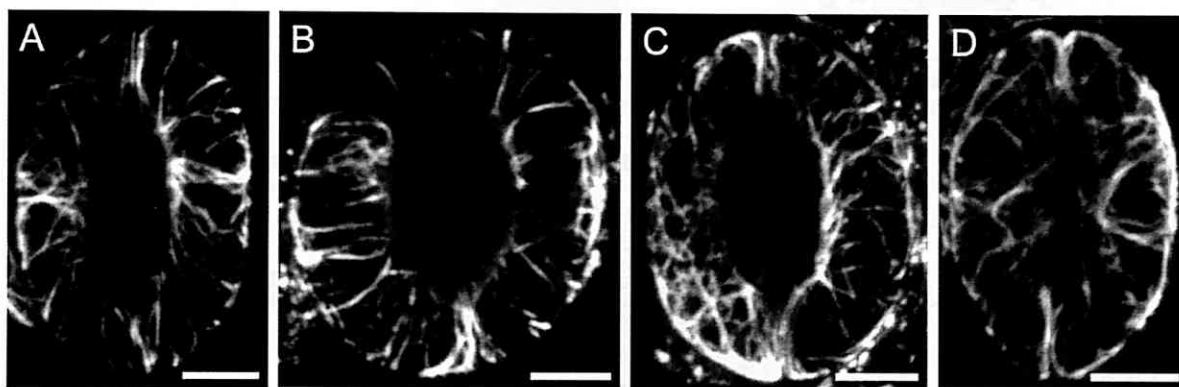


Fig. IV-1. Representative MF organization in guard cells of *Arabidopsis thaliana* at various times of the day. Images are maximum intensity projections from serial optical sections of GFP-ABD2-labelled MFs taken at 6:00 (A), 12:00 (B), 18:00 (C) and 0:00 hours (D) at 0.5 μm serial intervals. Scale bars: 5 μm .

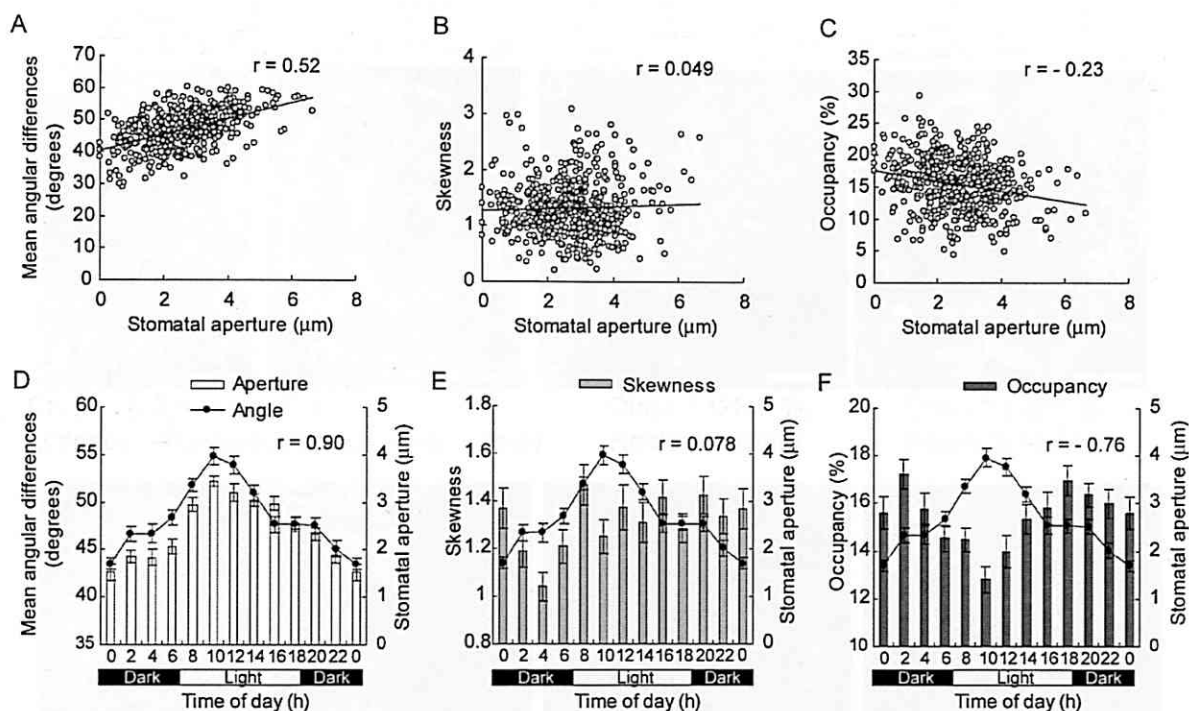


Fig. IV-2. Quantitative analysis of stomatal aperture, MF orientation, MF bundling, and MF density using microscopic image analysis. (A-C) Correlation analyses between stomatal apertures and MF orientation (A), MF bundling (B) and MF density (C). Data were plotted from 492 pairs of guard cells that were image-acquired throughout the diurnal cycle. (D-F) Diurnal changes in stomatal aperture and MF orientation (D), MF bundling (E) and MF density (F). Values are arithmetic means \pm SE from 38-45 independent pairs of guard cells. r indicates Pearson correlation coefficient.

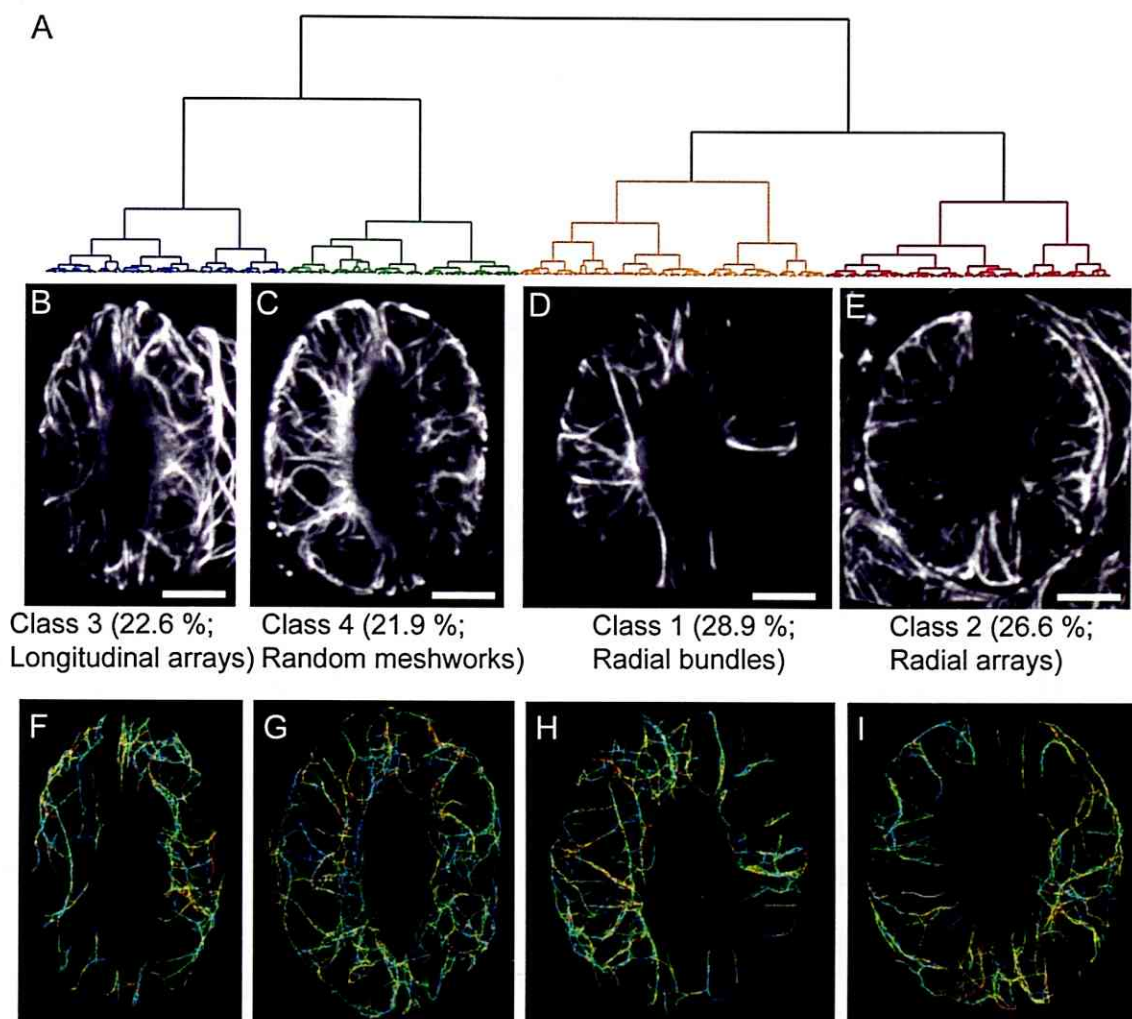


Fig. IV-3. Classification of MF configurations in guard cells of GFP-ABD2 expression lines. (A) Dendrogram of 492 MF configurations that were image-acquired throughout the diurnal cycle. The dendrogram was produced based on the patterns of the metrics of MF orientation, MF bundling and MF density using Euclid's algorithm and Ward's algorithm. (B-E) Representative images of class 1 "radial bundles" (D), class 2 "radial arrays" (E), class 3 "longitudinal arrays" (B), and class 4 "random meshworks" (C). Scale bars: 5 μ m. (F-H) The 3-D models of MFs in the longitudinal arrays (F), random meshworks (G), radial bundles (H) and radial arrays (I). The 3-D models were obtained using Modrec software that can be used to automatically reconstruct the 3-D fibrous structures from serial optical sections of fluorescently-labeled fibers using the point spread function.

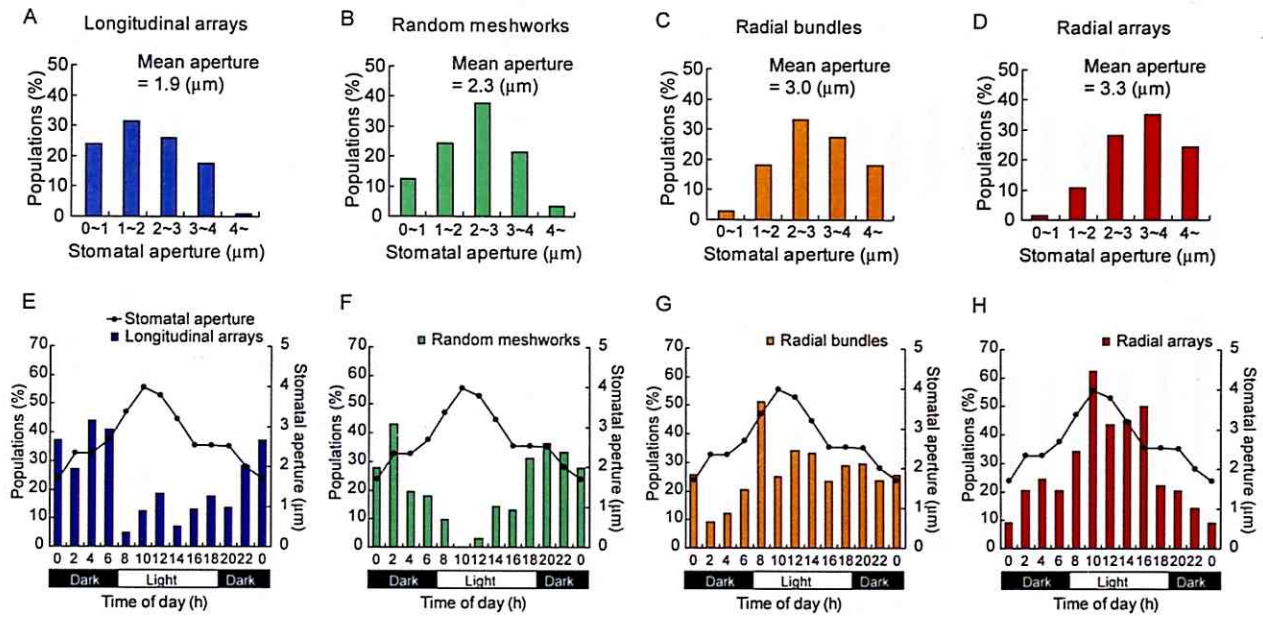


Fig. IV-4. Stomatal apertures and time of appearance of guard cells classified by MF configuration. (A-D) Histograms of stomatal apertures in guard cells with MF configurations classified as “longitudinal arrays” (A), “random meshworks” (B), “radial bundles” (C), and “radial arrays” (D). Population distributions were examined in 111 (A), 108 (B), 142 (C), and 131 (D) independent pairs of guard cells. (E-H) Diurnal changes in appearance frequency of guard cells with MF configurations classified as “longitudinal arrays” (E), “random meshworks” (F), “radial bundles” (G), and “radial arrays” (H). Populations were determined in 38-45 independent pairs of guard cells at each time point. Diurnal changes in mean values of stomatal apertures were merged as a line plot.

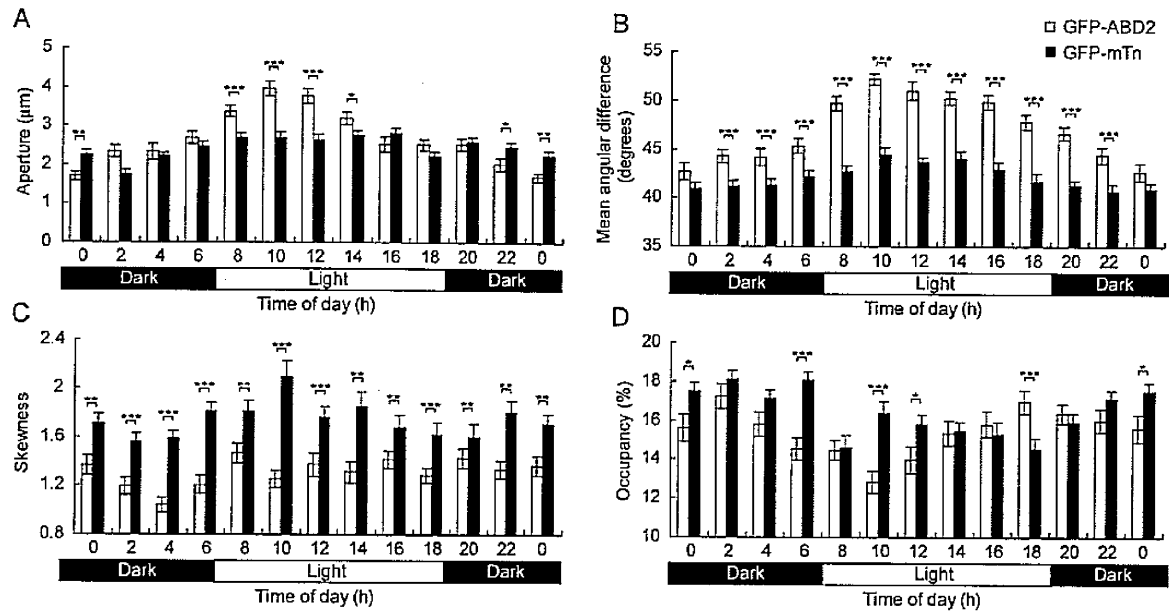


Fig. IV-5. Comparison of stomatal apertures and MF configurations between GFP-ABD2 and GFP-mTn expressing lines with diurnal cycles. Diurnal changes in stomatal apertures (A), MF orientation (B), MF bundling (C) and MF density (D) were examined in lines expressing GFP-ABD2 (open columns) or GFP-mTn (closed columns). Values are arithmetic means \pm SE from 38-50 independent pairs of guard cells. Significance was determined using Student's t-test. p -values * < 0.05 , ** < 0.01 , and *** < 0.001 .

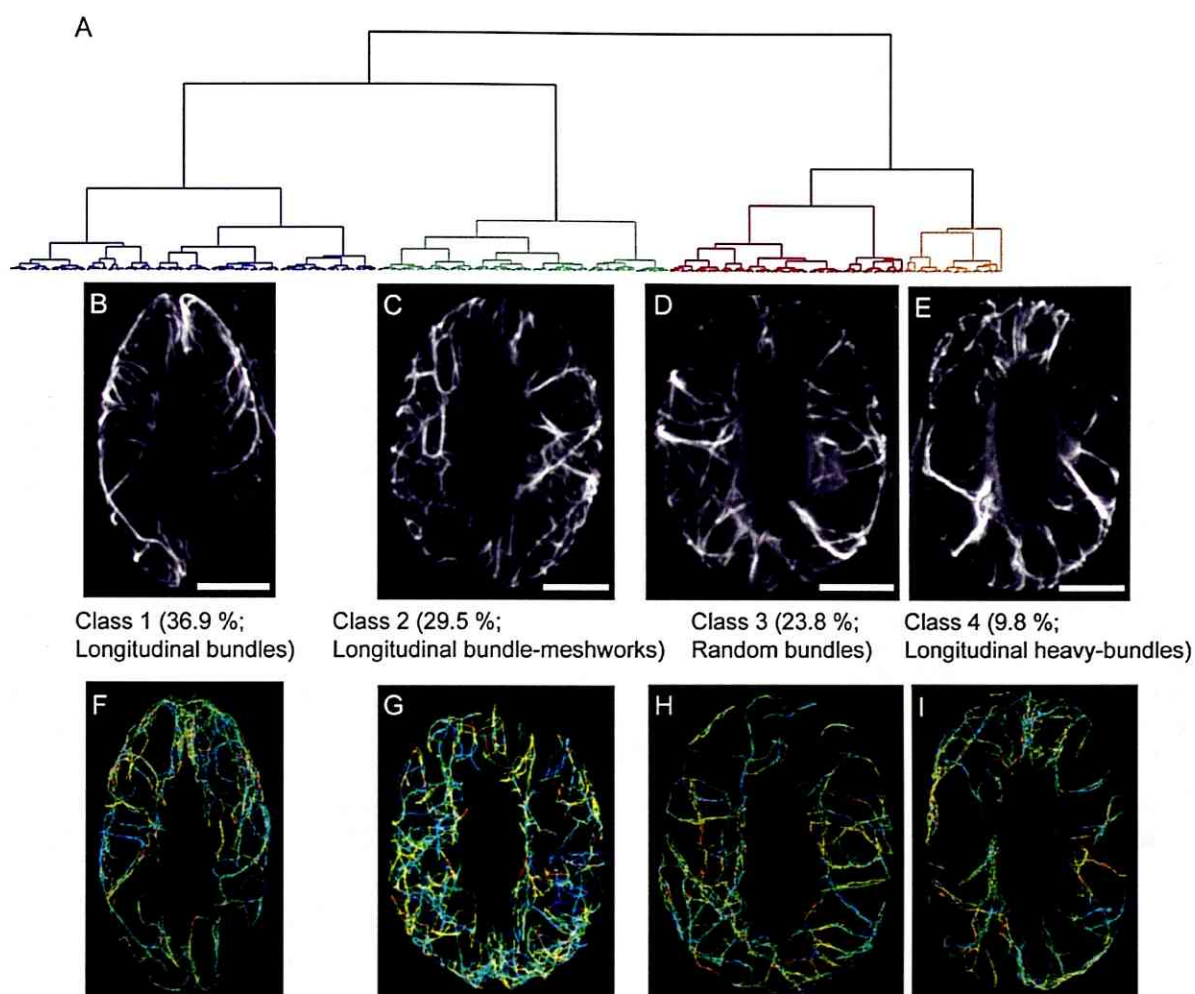


Fig. IV-6. Classification of microscopic images of guard cell MFs in GFP-mTn expression lines. (A) Dendrogram of 529 GFP-mTn-labeled MF configurations that were image-acquired throughout the diurnal cycle. The dendrogram was produced based on the pattern of the metric parameters of MF orientation, MF bundling and MF density using Euclid's algorithm and Ward's algorithm. (B-E) Representative images of class 1 “longitudinal bundles” (B), class 2 “longitudinal bundle-meshworks” (C), class 3 “random bundles” (D), and class 4 “longitudinal heavy-bundles” (E). (F-I) The 3-D models of MFs in longitudinal bundles (F), longitudinal bundle-meshworks (G), random bundles (H), and longitudinal heavy-bundles (I). The 3-D models were obtained using Modrec software.

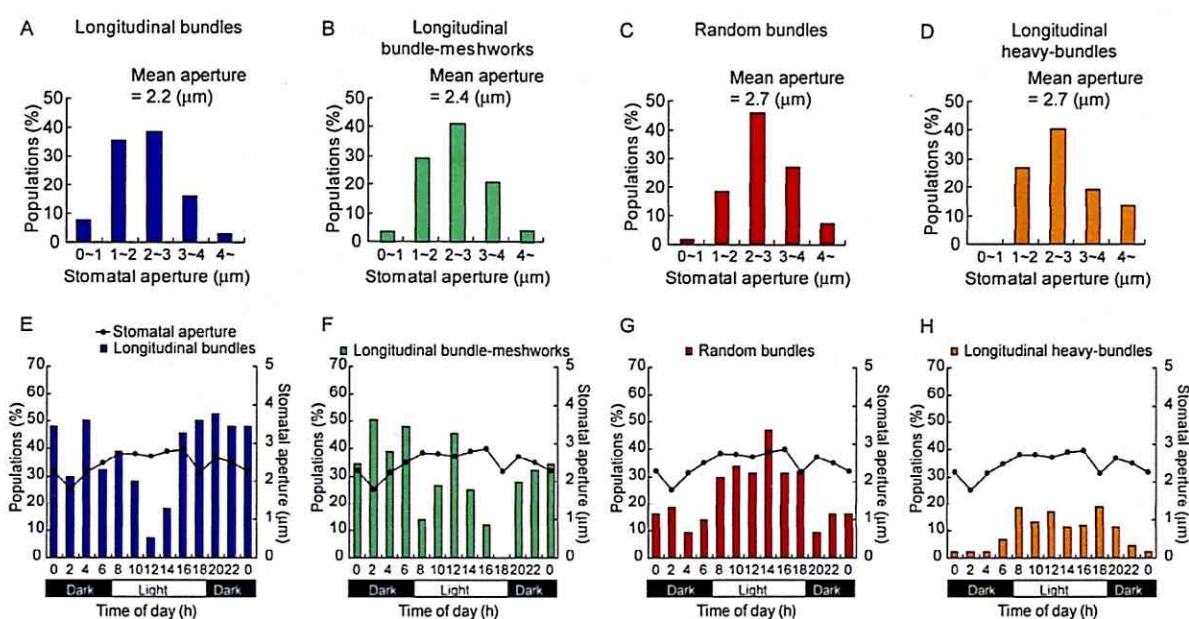


Fig. IV-7. Stomatal apertures and appearance time of guard cells classified by MF configurations in GFP-mTn expression lines. (A-D) Histograms of stomatal apertures in guard cells with MF configurations classified as “longitudinal bundles” (A), “longitudinal bundle-meshworks” (B), “random bundles” (C), and “longitudinal heavy-bundles” (D). The population distributions were examined in 195 (A), 156 (B), 126 (C), and 52 (D) independent pairs of guard cells. (E-H) Diurnal changes in appearance frequency of guard cells with MF configurations classified as “Longitudinal bundles” (E), “Longitudinal bundle-meshworks” (F), “Random bundles” (G) and “Longitudinal heavy-bundles” (H). Populations were determined in 40-50 independent pairs of guard cells at each time point. Diurnal changes in mean values of stomatal apertures were merged as a line plot.

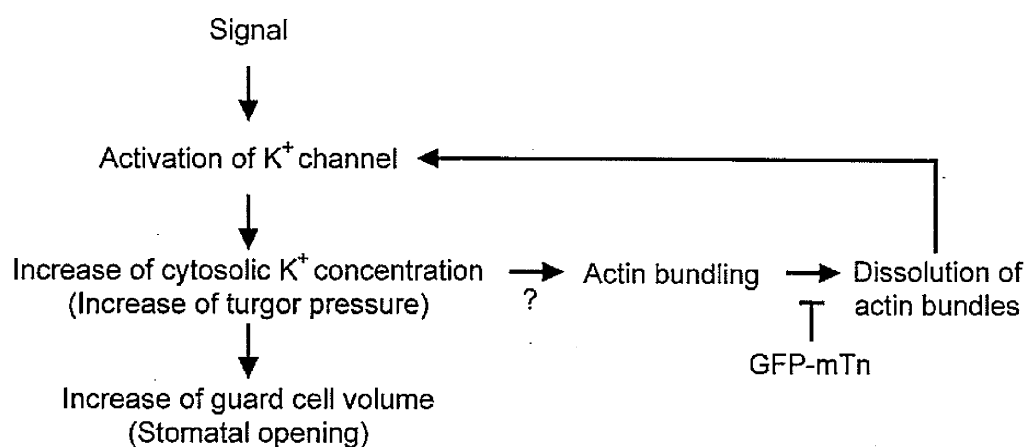


Fig. IV-8. Hypothetical model of the pathway by which MF dissolution promotes stomatal opening. The model is based on my observation that MFs are transiently bundled in the process of stomatal opening and from previous pharmacological findings that CD activates potassium channels (see Discussion for details). MFs are bundled after the increase in turgor pressure by unidentified mechanisms, and subsequent MF dissolution accelerates the increase in guard cell volume by activation of potassium channels. In the GFP-mTn expression lines, the dissolution is inhibited by GFP-mTn expression during the light period and so stomatal opening is suppressed.

Table IV-1.

Mean values of the metric parameters in each class.

	Mean angular difference (degrees)	Skewness	Occupancy (%)
GFP-ABD2 expression lines			
Radial bundles	50.3 \pm 4.2	1.83 \pm 0.45	15.8 \pm 3.8
Radial arrays	50.8 \pm 3.4	1.12 \pm 0.33	13.6 \pm 3.2
Longitudinal arrays	41.6 \pm 4.4	0.90 \pm 0.27	13.2 \pm 3.1
Random meshworks	43.5 \pm 4.0	1.36 \pm 0.36	19.8 \pm 2.7
GFP-mTn expression lines			
Longitudinal bundles	39.9 \pm 2.5	1.56 \pm 0.45	15.0 \pm 2.5
Longitudinal bundle-meshworks	41.8 \pm 2.0	1.63 \pm 0.49	20.0 \pm 1.7
Random bundles	46.3 \pm 2.2	1.59 \pm 0.48	14.4 \pm 3.0
Longitudinal heavy-bundles	42.7 \pm 2.4	3.36 \pm 2.13	13.7 \pm 3.3

Each class was determined by cluster analysis as shown in Figure IV-3, 6. Values are arithmetic means \pm SE, n=195-52.

Suppelemental figures

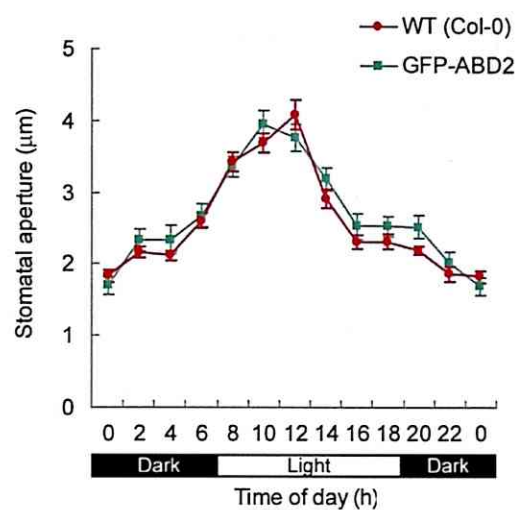


Fig. IV-S1. Diurnal cycles of stomatal movement in wild-type (WT) and GFP-ABD2 (GF1-3) expressing *Arabidopsis* plants. Values are arithmetic means \pm SE from 38-45 independent pairs of guard cells.

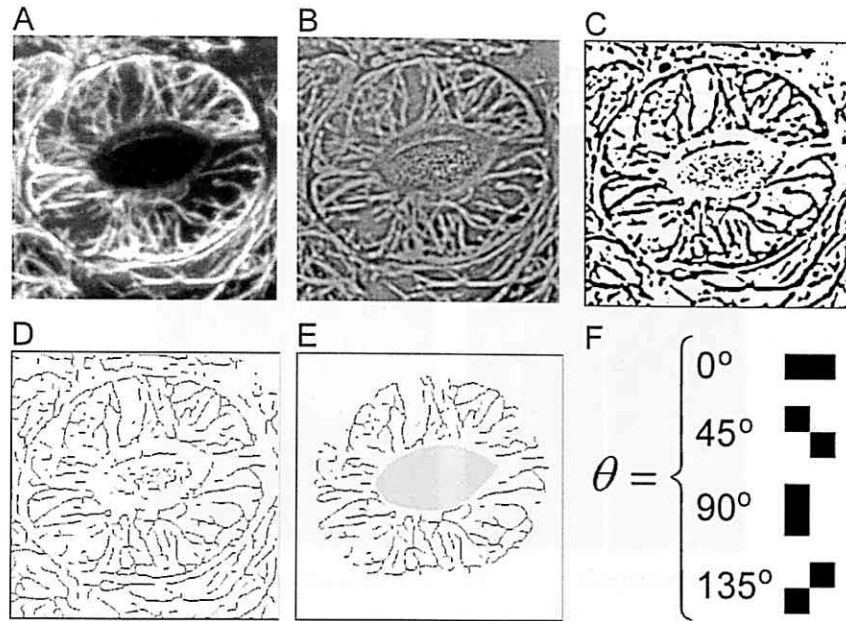


Fig. IV-S2. Scheme of image processing to quantitatively evaluate MF orientations. I first obtained a maximum intensity projection constructed from serial optical sections of MFs (A). To perform noise reduction and skeletal enhancement, a 5-10 pixel-band-pass filter was applied (B). The image was then binarized by thresholding (C) and thereafter skeletonized (D). Black pixels were defined as MF pixels. After elimination of MF pixels in non-guard cells, the stomatal pore region (gray region), that was manually segmented, was merged (E). I measured the mean angular difference between MF pixel pairs and the nearest pixel pairs of stomatal pore edges as an indicator of MF orientation (see Methods). MFs with a perfect radial orientation have the highest mean angular difference of 90°, and MFs with a perfect longitudinal orientation have the lowest mean angular difference of 0°. (F) Discretization of angles of pixel pairs. The angles of pixel pairs, which were used to calculate the mean angular difference as described in Methods, are categorized into 0, 45, 90 and 135°.

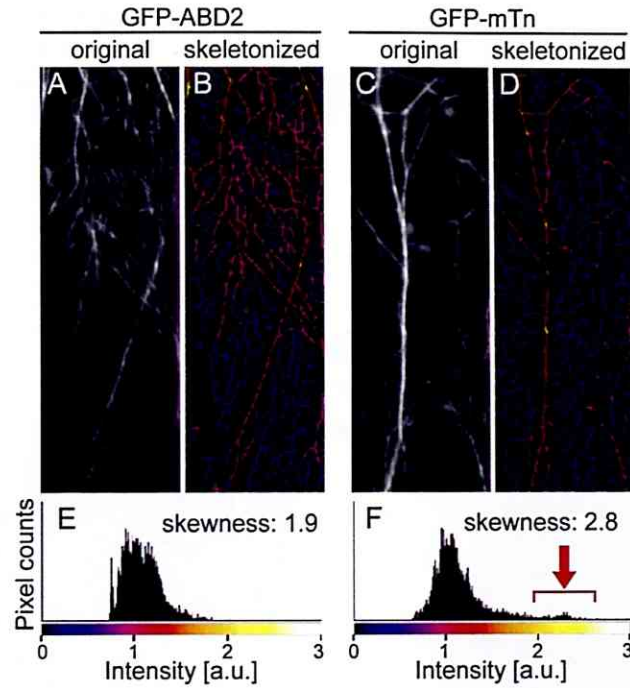


Fig. IV-S3. Quantitative evaluation of MF bundling. As an example, MF images in *Arabidopsis* hypocotyl cells expressing GFP-ABD2 (A) and GFP-mTn (C) were used. To collect pixels constituting MFs, I obtained the skeletonized images (B, D). Intensities of skeletonized MF pixels are shown by pseudo colors. As visualized by the intensity histograms, the number of high intensity pixels in the skeletonized image of GFP-mTn-labelled MF bundles (F, red arrow) is greater than that in the image of the GFP-ABD2-labelled MF array (E). When the high intensity pixel numbers increase, the skewness of the intensity distribution (see Methods for definition) becomes higher.

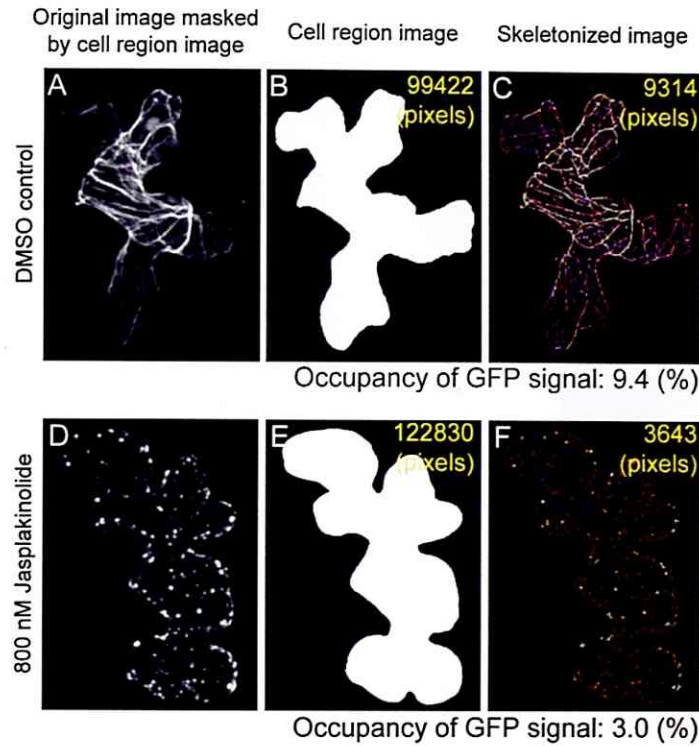


Fig. IV-S4. Quantitative evaluation of MF density. As an example, MF images in GFP-ABD2 expressing *Arabidopsis* leaf epidermal cells treated with DMSO control (A) and 800 nM Jasplakinolide (D) for 1 hour were used. I firstly manually segmented the cell region and measured the pixel numbers constituting the cell region (B, E). Subsequently, the MF pixels were extracted by skeletonization and the pixel numbers counted (C, F). The occupancy, defined by the percentage of pixel numbers constituting the skeletonized MFs in the total pixel numbers of the cell region (see also Methods), becomes lower when MFs are depolymerized or fragmented.

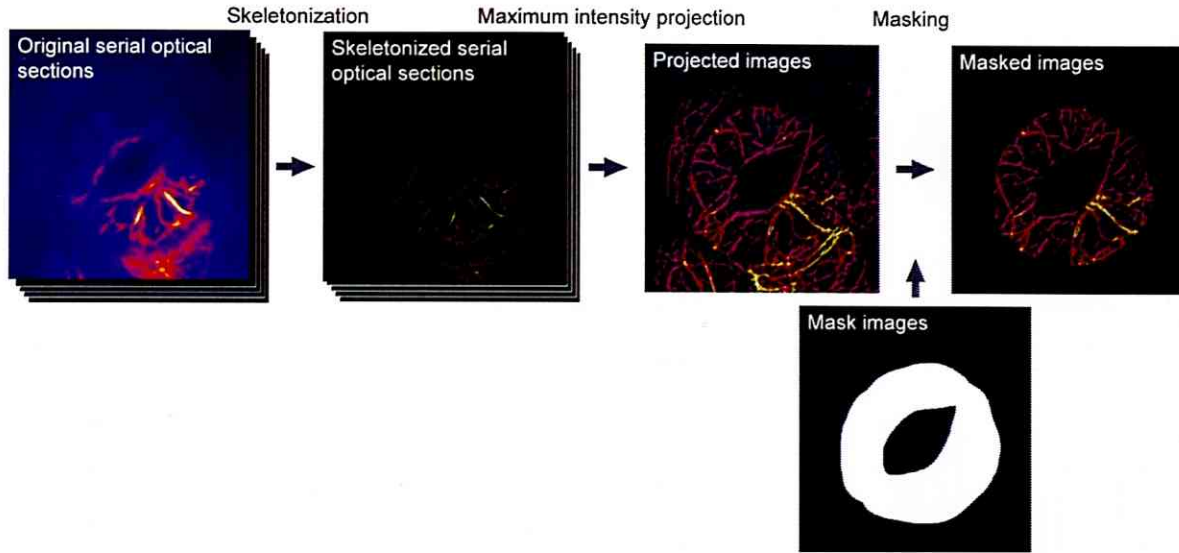


Fig. IV-S5. Preprocessing of quantitative evaluation of MF bundling and density in guard cells. From the original serial optical sections, I first obtained skeletonized images that were then projected by maximum intensity projection and masked by manually-segmented cell region images. The masked images were used for quantitative evaluation of MF bundling and density.

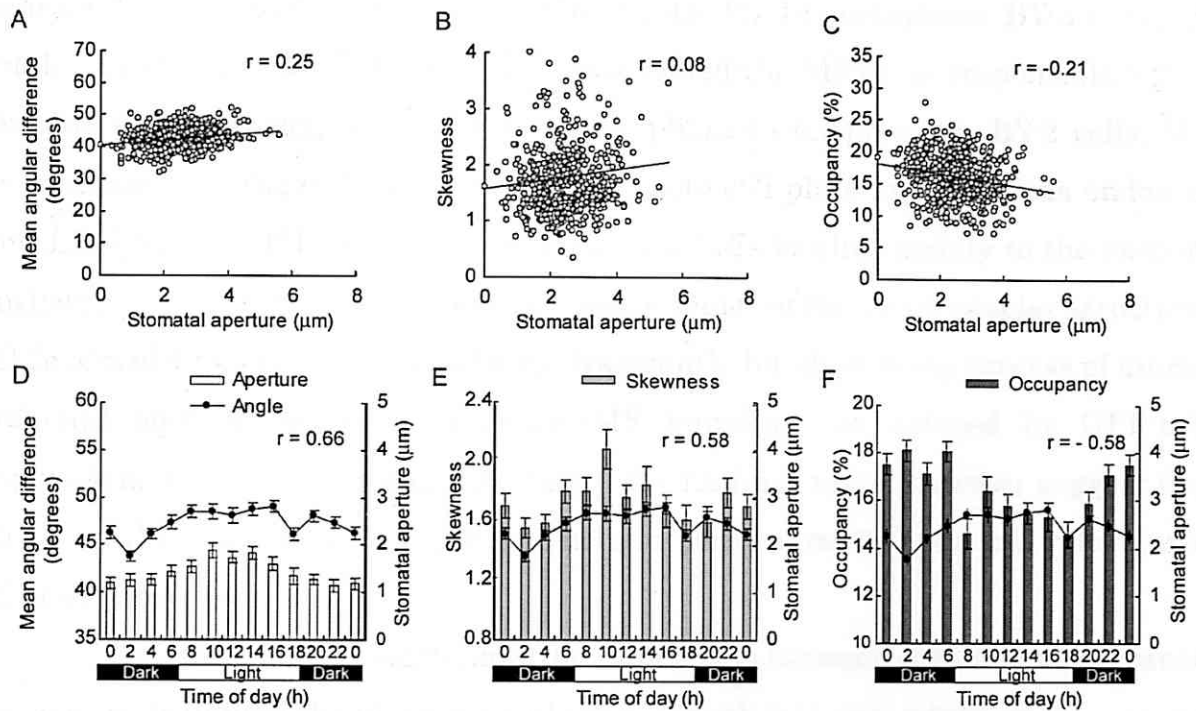


Fig. IV-S6. Quantitative analysis of stomatal aperture, MF orientation, MF bundling, and MF density in GFP-mTn expressing lines. (A-C) Correlation analyses between stomatal apertures and MF orientation (A), MF bundling (B) and MF density (C). Data were plotted from 529 pairs of guard cells that were image-acquired throughout the diurnal cycle. (D-F) Diurnal changes in stomatal aperture and MF orientation (D), MF bundling (E) and MF density (F). Values are arithmetic means \pm SE from 40-50 independent pairs of guard cells. r indicates Pearson correlation coefficient.

General conclusions and perspectives

In this study, I have investigated the dynamics and roles of MFs in plant cell morphogenesis by live imaging of tobacco BY-2 cells and in *Arabidopsis thaliana* guard cells. I found some remarkable events: (1) In metaphase BY-2 cells, the establishment of two MF meshwork bands, called the MFTP, is responsible for cell division plane determination; (2) From anaphase to telophase in BY-2 cells, MFs accumulate near the cell plate and they promote cell plate expansion via endosome and ER dynamics; (3) In interphase BY-2 cells, MFs localize mainly to the vacuolar surface and MF-disruption impairs the maintenance of the intravacuolar structures; (4) In *Arabidopsis* guard cells, MFs are transiently bundled in the process of diurnal stomatal opening, whereas excessive MF bundling, as induced by GFP-mTn expression, suppresses stomatal opening. My findings taken together suggest that, based on the cell status, MFs reorganize and perform multifunctional roles during cell morphogenesis.

Importantly, my studies show the interaction between MFs and membranous structures, including the plasma membrane, endoplasmic reticulum, endosomes and vacuoles. Since these membranous structures are sensitive to cell fixation procedures, previous MF visualization techniques may have overlooked these interactions. The colocalization of several actin-side binding proteins and the motor protein, myosin, on the membranous structures has been reported (reviewed by Higaki et al. 2007). In the near future, *in vivo* multiple labeling of both MFs and actin-side binding proteins, together with high-speed multicolor imaging and the use of mutants with MF functions, will provide new insights into the molecular mechanisms of actin-based plant cell morphogenesis.

Reference

Higaki T, Sano T, Hasezawa S. (2007) Actin microfilament dynamics and actin side-binding proteins in plants. *Curr. Opin. Plant Biol.* 10:549-556.